



Facultad
de
Ciencias

Second principles simulation of the electronic state of CuO_2 layers

Simulación de segundos principios del estado electrónico de láminas
de CuO_2

Trabajo de Fin de Grado
Para acceder al
GRADO EN FÍSICA

Autor: Guillermo Ruiz Laborda
Director: Pablo Garcia-Fernández

Junio - 2020

*A mi abuela Paquita,
sé que estarías orgullosa.*

Agradecimientos

En primer lugar, me gustaría agradecer el apoyo y la atención del tutor de este trabajo, Pablo García-Fernández. No solamente quiero hacer destacar su disposición para ayudarme y resolver las dudas que me iban surgiendo, sino también su actitud de cara a dirigirme un proyecto en el que me ha dado libertad para hacer algo propio y genuino. Además, me gustaría mencionar el papel del profesor Jose Antonio Aramburu-Zabala, cuya asignatura me llevó a interesarme por la Física de Estado Sólido y elegir este tema para el trabajo.

A nivel personal, son demasiadas las personas que han pasado por mi vida estos últimos cinco años y que han hecho de este período algo especial. Por supuesto, agradezco a mi grupo de amigos previo a mi etapa universitaria el haber estado siempre ahí y poder pasar tan buenos momentos con ellos. En particular, a Celia, por haberme enseñado tanto.

Mis compañeros de Facultad han sido también muy importantes, me han enseñado tanto el valor del esfuerzo y el trabajo como la necesidad de disfrutar de estos años y afrontar la vida con más optimismo. De aquí, quería nombrar a Nacho y a Íñigo, sin los cuales mi paso por esta Facultad no habría tenido mucho sentido.

Fuera de Santander, tanto en Berlín como en Suiza, he conocido a gente muy especial. Me habéis enseñado a ser más independiente y a atreverme a cosas que antes ni imaginaba. De vosotros me queda el recuerdo de dos experiencias inolvidables.

Y, por supuesto, quedaba agradecer todo esto a mi familia, siempre apoyándome y animándome tanto en el plano académico como en el personal. Gracias a mis padres, Antonio y Carmen, por hacer de mí la persona que soy hoy en día.

Abstract

The phenomenon of superconductivity was firstly observed over one century ago, and since then it has become one of the most important fields of study of Solid State Physics. For decades, the BCS theory was able to explain the mechanism that leads to this phenomenon in certain compounds, called conventional superconductors. However, the discovery of high-temperature superconductivity in 1986 by Bednorz and Müller evidenced that the BCS theory itself, and still no one, is capable to wholly explain superconductivity.

In this work, we have studied the electronic structure of CuO_2 layers like those appearing in La_2CuO_4 , one of the reference materials for high-temperature superconductivity. These cuprate superconductors exhibit a characteristic phase diagram with hole doping and temperature as axes. By means of a simple model, combining both second-principles techniques and a Markov Chain Monte Carlo, we have focused on the region of the aforementioned phase diagram where the system is not doped with holes. These elements combined have served us to computationally reproduce a simultaneous antiferromagnetic-paramagnetic and insulator-metal phase transition.

Keywords: High-temperature superconductivity, La_2CuO_4 , second-principles, Markov Chain Monte Carlo, spin correlation, phase transition.

Resumen

El fenómeno de la superconductividad fue observado por primera vez hace más de un siglo, y desde entonces se ha convertido en uno de los campos de estudio más importantes de la Física de Estado Sólido. Durante décadas, la teoría BCS fue capaz de explicar el mecanismo que causa este fenómeno en un cierto número de compuestos, llamados superconductores convencionales. Sin embargo, el descubrimiento de la superconductividad de alta temperatura en 1986 por Bednorz y Müller evidenció que la teoría BCS por sí misma, y aún hoy día ninguna, es capaz de explicar completamente la superconductividad.

En este trabajo, hemos estudiado la estructura electrónica de láminas de CuO_2 como las que aparecen en La_2CuO_4 , uno de los superconductores de alta temperatura de referencia. Estos cupratos superconductores presentan un diagrama de fase característico cuyos ejes son el dopaje con huecos y la temperatura. Por medio de un modelo sencillo, combinando tanto técnicas de segundos principios como un método Monte Carlo de cadena de Markov, nos hemos centrado en la región del mencionado diagrama de fases en donde el sistema no está dopado con huecos. La combinación de estos elementos nos ha servido para reproducir, computacionalmente, una transición de fase simultánea: antiferromagnético-paramagnético y aislante-metal.

Palabras clave: Superconductividad de alta temperatura, La_2CuO_4 , segundos principios, Monte Carlo de cadena de Markov, correlación de spin, transición de fase.

Contents

1	Introduction	1
1.1	Superconductors	1
1.2	High temperature superconductors	4
1.2.1	La_2CuO_4 - Reference material for high- T_c superconductivity	5
1.2.2	Phase diagram (T,doping) in La_2CuO_4	7
1.3	Objectives of this work	8
1.4	Structure of this work	9
2	Computational methods	11
2.1	First principles methods	12
2.1.1	Notation	12
2.1.2	Hamiltonian	12
2.1.3	Adiabatic approximation	13
2.1.4	Electronic hamiltonian	14
2.1.4.1	Hartree-Fock method	14
2.1.4.2	DFT	16
2.1.4.2.1	Hohenberg-Kohn Theorems	17
2.1.4.2.2	Kohn-Sham approach	18
2.2	Second-principles methods	20
2.2.1	Overview of SP-DFT	20
2.2.2	Energy in SP-DFT	21
2.3	Effective form of the SP Hamiltonian in this work	22
2.3.1	Tight-binding model	22
2.3.2	Two-electron interactions: Hubbard model	23
2.4	Monte Carlo method and implementation in this work	25
3	Results	29
3.1	Model employed	29
3.2	FM vs AFM	30
3.3	Importance of U/γ	32
3.4	Correlation as function of energy. Microstates	34
3.5	AFM insulator - paramagnetic metal phase transition during MC	37
4	Conclusions and future work	43
	Bibliography	45
A	Code implementation	47

Chapter 1

Introduction

Superconductivity is one of the most important phenomena in Solid State Physics. Despite being discovered over one century ago and having theoretical foundations set 30 years afterwards, there are still many aspects that are not fully understood. In particular, the discovery of high-temperature superconductors and their behaviour is still a source of intense debate. In this work, we will delve into the phase diagram of La_2CuO_4 , the original high-temperature superconductor, trying to understand part of its intricate electronic properties by means of a simple computational model.

In this chapter, we shall begin by introducing fundamental concepts in order to provide the reader with a brief overview of the problems of superconductors and their phenomena that will appear in subsequent chapters. After this, we will introduce the phenomenon of high-temperature superconductivity, particularizing the case of La_2CuO_4 . We will continue by discussing the phase diagram (temperature, doping) of this material and indicating the region which will be the focus of this work. Finally, we will briefly explain the importance of the first-principles simulations in the frame of Condensed State Physics, stating our objectives for the present work.

Contents

1.1 Superconductors	1
1.2 High temperature superconductors	4
1.2.1 La_2CuO_4 - Reference material for high- T_c superconductivity	5
1.2.2 Phase diagram (T,doping) in La_2CuO_4	7
1.3 Objectives of this work	8
1.4 Structure of this work	9

1.1 Superconductors

It is well known from the experiments that applying a static electric field \vec{E} on a metallic sample produces a current density given by Ohm's Law [1]:

$$\vec{J} = \sigma \vec{E}, \tag{1.1}$$

where σ is the electric conductivity, characteristic of the material (Note that σ is in fact a second order tensor). We also define the resistivity $\rho = 1/\sigma$ as its inverse. For a wire of length L and section A , we may define the resistance as

$$R = \frac{L}{A}\rho \quad (1.2)$$

so that the Ohm's Law takes a much simple form in terms of the current I and the voltage V ,

$$I = \frac{V}{R}. \quad (1.3)$$

The dependence of ρ on temperature is not trivial, and it varies depending on whether we are analysing the case of a metal (the electrons of the conduction band behave as nearly free electrons) or a semiconductor (it is necessary to take into account the electrons of both the conduction and the valence bands). Essentially, the main factors that account for resistivity are lattice vibrations (phonons), electron-electron interactions and crystallographic defects. At sufficiently low temperatures, only the last contribution and the zero point vibration show up, leading to a constant resistivity value.

At the beginning of the 20th century, Solid State Physics was in its infancy, and physicists were quite interested in resistivity's dependence with temperature. One of those physicists, a man called Heike Kamerlingh Onnes, was the first person to liquefy Helium in 1908, being able to work at temperatures of about 4 K.

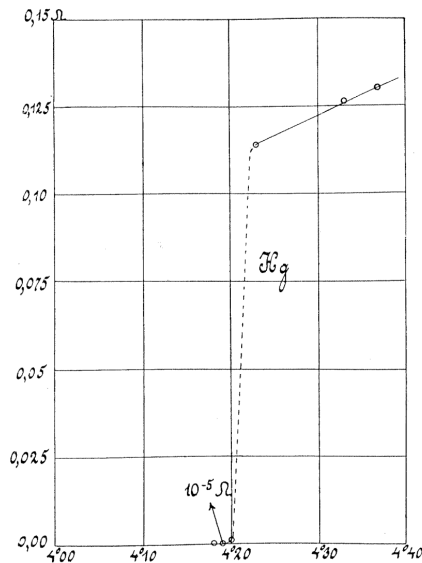


Figure 1.1: Original experiment result from Kamerlingh Onnes depicting the resistivity's dependency of temperature in Hg. Ref: [3].

In 1911, he undertook such a study at low temperatures, choosing a Mercury sample which he had obtained in a sufficiently pure form [2]. Kamerlingh Onnes discovered the phenomenon of superconductivity, noting that the resistance of his sample abruptly dropped to almost zero at a temperature of 4.2 K (see figure 1.1). Moreover, he made sure that adding impurities to the sample did not hinder this to happen. From Kamerlingh Onnes onwards, the temperature below which the material enters a superconducting phase is called critical temperature (denoted by T_c), whose magnitude for conventional superconductor is of the order of some Kelvin (until the discovery of high- T_c superconductors [7] no material displayed a T_c higher than 23 K). This discovery was one of the most outstanding breakthroughs in Physics, opening the door for a new and important branch in Solid State Physics.

Superconductors exhibit both exotic electric and magnetic properties. On one hand, no energy is dissipated as a consequence of the Joule effect, thus resulting in currents that can be indefinitely maintained and transported without any losses. On the other hand, superconductors exhibit perfect diamagnetism, i.e., they are characterized by a total absence of permeability and a magnetic susceptibility of $\chi = -1$. In other words, magnetic field lines are expelled from the superconductor's surface due to the presence of supercurrents upon it. Named after its discoverer, the German physicist Walter Meissner, this phenomenon is generally known as **Meissner effect** (cf. Fig. 1.2).

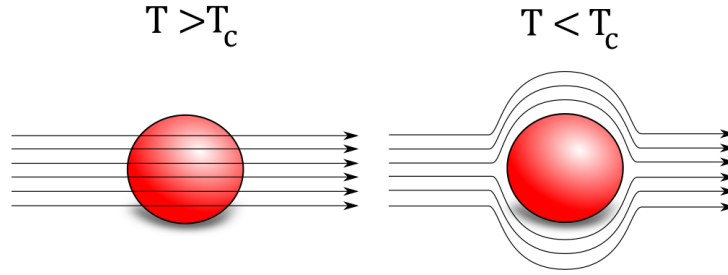


Figure 1.2: *Magnetic field lines are excluded from a superconductor below its critical temperature (right).*

The first and best known microscopic theory of superconductors is the BCS theory, named after John Bardeen, Leon Cooper and John Robert Schrieffer [4]. John Bardeen came to realize that phonons produce an attractive interaction between electrons close to the Fermi surface. The main idea behind the BCS theory is that this attraction, even if small, leads to the formation of electron pairs, called **Cooper pairs**. Classically, this behaviour may be explained by the following reasoning: a moving electron attracts positive charged ionic nuclei, thus creating a slightly more positive charge density around the electron. Other electron nearby will be partially attracted by this region with positive charge. The net effect can be seen *as if* the second electron were attracted by the first one, thus allowing us to consider a bound pair as a some kind of quasiparticle.

Although each electron is a fermion with spin-1/2, the pair treated as a whole is a spin 1 or 0 particle, and hence it does not longer obey Fermi-Dirac Statistics. Pairs of electrons have integer spin and can condensate into the same energy level, having at the end of this process a slightly lower energy than unpaired electrons would have. The condensed electrons leave an energy gap

$$E_g \approx \frac{7}{2} k_B T_c$$

above them. This energy gap hinders collisions that cause the ordinary resistivity. For temperatures associated with a thermal excitation smaller than the band gap, the material exhibits zero resistivity. This behaviour allows this theory to confidently explain the Meissner effect and critical temperature. This condensation might seem as a Bose-Einstein condensation as mentioned in literature (cf. for example the original article [4]), although rigorously speaking this is a system made up of fermions and thus the situation is not completely analogous.

The BCS theory was derived from the physical idea of coupling between the movement of electrons and nuclei, commonly known as electron-phonon coupling. However, the same idea of weak coupled pairs may be applied to other pairing mechanisms. For example, the BCS theory has contributed to the development of the Higgs mechanism that accounts for the mass generation of fundamental particles [6].

Generally speaking, the BCS theory is capable to explain the phenomenon of superconductivity in some materials, although it is still unable to give answers to what happens in many others. That is the reason why the BCS theory is not considered to be a closed theory of the superconductivity. One of the main issues arising when discussing this phenomenon is the existence of high-temperature superconductors.

1.2 High temperature superconductors

High-temperature superconductors may be defined as those whose critical temperature is above 23 K (the highest temperature reached until the discovery of La_2CuO_4). With this term we may refer to those superconductors that do not obey the BCS theory (usually known as conventional superconductors), which in general turn out to have a higher critical temperature than those that can be explained by the aforementioned theory. However, there are conventional superconductors that present a high T_c , such as some hydrides [5].

High temperature superconductivity was first discovered by Bednorz and Müller in 1986 in La_2CuO_4 doped with Ba. Nowadays, the Sr-doped family of compounds $La_{2-x}Sr_xCuO_4$ is a broadly studied field because of its remarkable usefulness to understand high-temperature superconductivity. Right after Bednorz and Müller, it was found that doping with Sr raised the superconducting critical temperature T_c of La_2CuO_4 to almost 40 K [9].

The more recent discovery in 2006 of the iron-based superconductors has been, together with the contribution of Bednorz and Müller in 1986, another milestone for the high T_c superconductivity (see Figure 1.3).

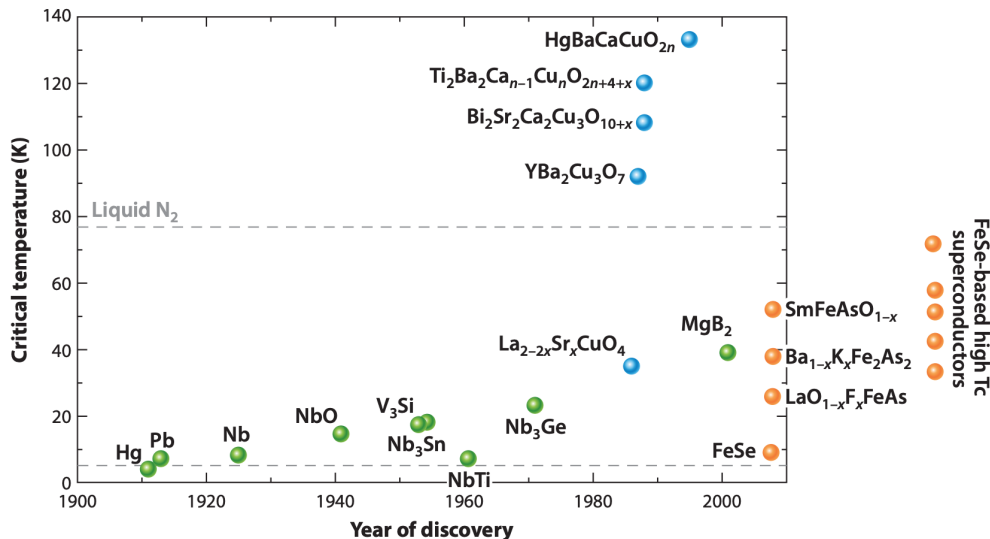


Figure 1.3: Critical temperatures for representative materials exhibiting superconductivity plotted as a function of the year of discovery. Conventional superconductors (explained by BCS) are displayed in green. Blue and orange dots stand for copper-oxide and iron-based superconductors, respectively. The right-most vertical array of orange dots represents the recently discovered FeSe-based bulk and interface superconductors. Reference: [7].

As already mentioned, the BCS theory does not suffice to explain high- T_c superconductivity. According to Ref. [7, p.262], this theory is based upon a generic instability of the *Fermi liquid*, a theoretical model of interacting fermions with screened Coulomb repulsion that describes conventional metallic states for sufficiently low temperatures. In this situation, any weak attractive interaction, not limited to lattice vibrations, sparks the formation of Cooper pairs.

Nevertheless, many high T_c materials behave as “strange metals” before becoming superconducting, meaning that their resistivity depends linearly on temperature when it should be quadratically [16]. It is hence crucial to understand the properties of strange metals and to what extent they are susceptible to Cooper pairs formation, not to mention whether Cooper pairing is the only Fermi

liquid's instability leading to superconductivity.

1.2.1 La_2CuO_4 - Reference material for high- T_c superconductivity

Most high- T_c superconductors present a common feature: Two-dimensional CuO_2 layers. However, whereas the structure of La_2CuO_4 is quite simple, that of higher- T_c superconductors turns out to be more intricate. Let us see it in detail.

La_2CuO_4 consists of alternating LaO and CuO_2 layers as seen in Fig. 1.4. Copper atoms are surrounded by six O, forming a distorted octahedral complex. At high temperatures, this material has the same tetragonal structure as K_2NiF_4 , with a space group $I4/mmm$. Below a temperature of 530 K, undoped La_2CuO_4 adopts a new orthorhombic symmetry, space group $Bmab$, because of tilt CuO_6 octahedra (See figure 1.4).

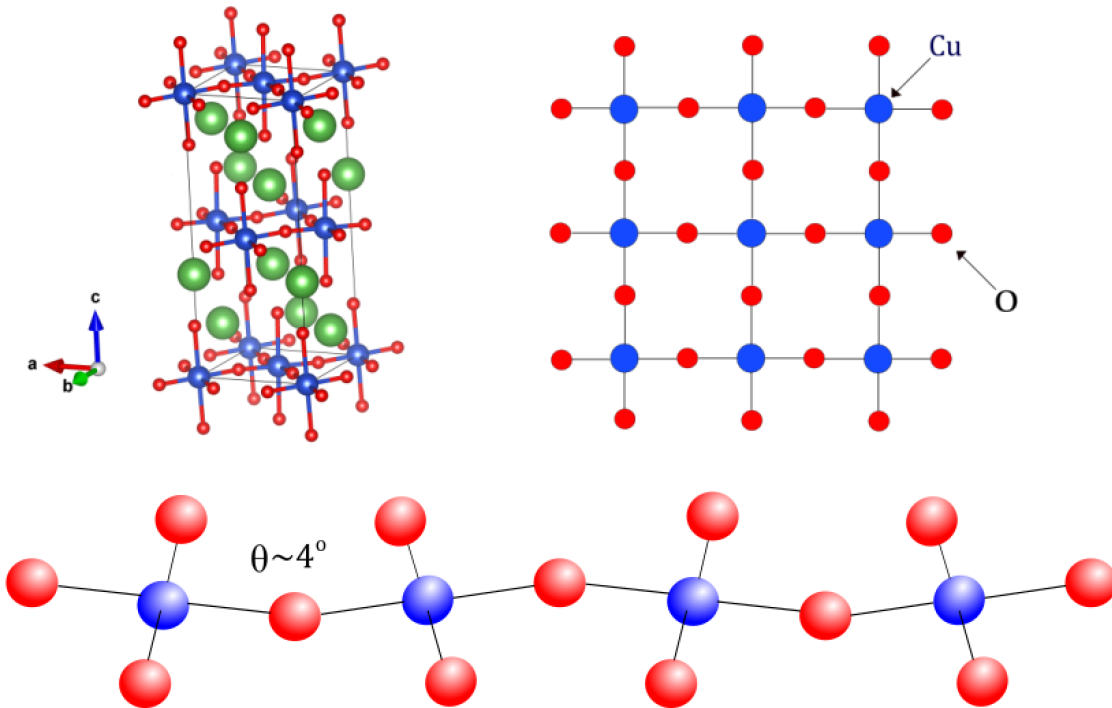


Figure 1.4: Graphical depiction of the La_2CuO_4 structure (upper left), performed with VESTA, and the CuO_2 layers (upper right). This structure corresponds to that of the orthorhombic system, found at room-temperature and below 530 K. The octahedra present a small tilting angle of about 4° (down).

The room-temperature lattice constants for La_2CuO_4 are $a = 5.354 \text{ \AA}$, $b = 5.401 \text{ \AA}$ and $c = 13.153 \text{ \AA}$ [9]. The tilt angle of the octahedra is about 4° . Hereinafter, in order to simplify the geometry and make full use of symmetry, we will neglect this small angle and assume that the structure is tetragonal.

Let us now focus on how to describe the electronic structure of the CuO_2 layers. If we start by considering an isolated cation Cu^{2+} , it is well known that the atomic configuration is $[Ar] 3d^9$. Hence, there is an unpaired electron inside of five $3d$ degenerate orbitals. For the sake of this work, let us consider a Cu^{2+} surrounded by six O^{2-} forming a CuO_6^{10-} complex. We will consider this compound's symmetry to be perfectly octahedral just for this analysis, hence presenting O_h sym-

metry. We may perform a qualitative analysis on this complex analogously to many others, such as the CrO_6^{3-} or the CuF_6^{4-} , just to mention some of them.

The five $3d$ degenerate orbitals of the isolated ion split into a triplet $t_{2g}(xy, xz, yz)$ and a doublet $e_g(x^2 - y^2, z^2)$, irreducible representations of the O_h group. The e_g orbitals present a stronger σ -antibonding character and thus higher energy than t_{2g} ones, which have π -antibonding character. Therefore, the $e_g - t_{2g}$ energy split is caused by the difference in bonding character appearing between these orbitals in O_h symmetry.

Now, let us go further. There is a quite sensitive issue here when we are faced with the explanation of the actual symmetry of a CuO_6^{10-} complex in La_2CuO_4 . One may easily find in literature that this complex, since its doublet e_g presents an orbital degeneration, undergoes a spontaneous symmetry breaking in the form of a tetragonal distortion, known in this case as Jahn-Teller effect. However, this explanation, though apparently general and reasonable, is **not true**. The reason is that this system does not display a cubic structure and thus an usual Jahn-Teller effect cannot be applied (for more detail, cf. [11]). Instead, the orbital ordering can be explained by means of the internal electric field over electrons localized in the complex, a fact commonly ignored.

In our case, it is straightforward to see that the LaO layers, positively charged, attract the electrons in $3d_{z^2}$ orbitals, whose two lobes are pointing towards the z axis. This stabilizes the orbital, which becomes doubly occupied. Given that the gap between the mainly $x^2 - y^2$ and z^2 orbitals is large enough, we can just consider the former one as it is partially occupied (see Figure 1.5).

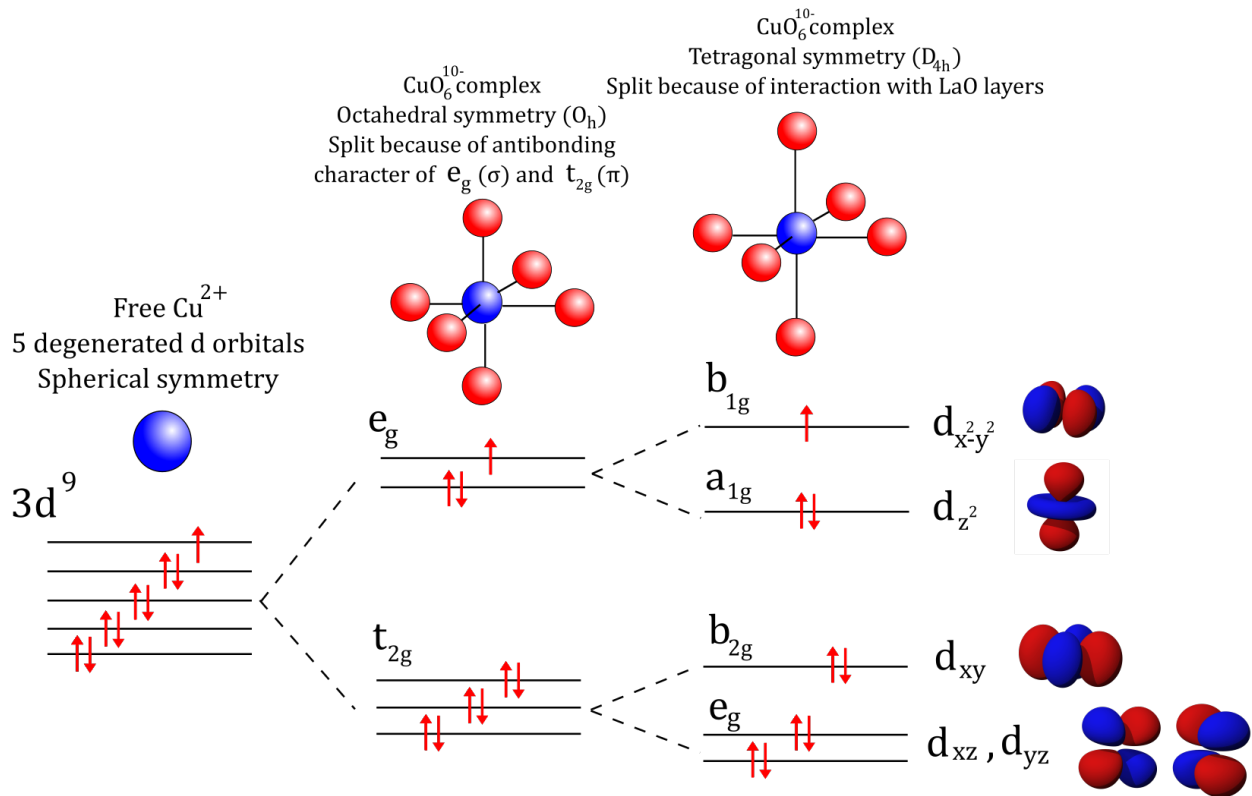


Figure 1.5: Representation of the orbital ordering of the $Cu-O$ octahedra in La_2CuO_4 . It turns out that the ground state presents a $d_{x^2-y^2}$ orbital, whose geometry lays on the CuO_2 layer.

On the other hand, it is clear that on the CuO_2 layers there are relevant p_x and p_y orbitals from the oxygen, as depicted in Figure 1.6. These orbitals overlap strongly with the $d_{x^2-y^2}$ metal orbitals and hybridize with them. In this work we will consider Wannier functions that effectively take this hybridization into account.

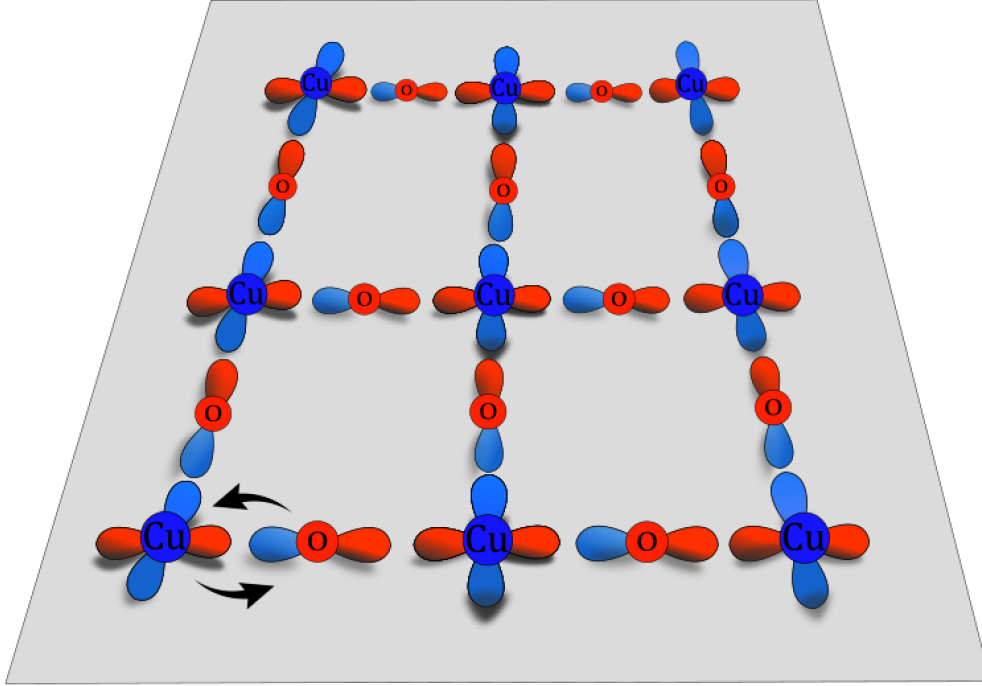


Figure 1.6: CuO_2 layer, both $Cu^{2+} d_{x^2-y^2}$ as well as $O^{-2} p_x, p_y$ orbitals are depicted.

The p_z orbital, pointing towards the z axis, might be important as well. However, it does not overlap with the $x^2 - y^2$ orbital, so we will neglect it.

1.2.2 Phase diagram (T,doping) in La_2CuO_4

A quite thorough way to characterize the behaviour of superconducting cuprates, like La_2CuO_4 , is through their phase diagram. It turns out that the phases these materials display essentially depend on both temperature T and doping concentration x . The underlying ideas behind this diagram are crucial to understand the phenomenon of superconductivity in cuprates.

For the sake of simplicity, let us consider a generic high- T_c superconductor's phase diagram to be applied on La_2CuO_4 . Hereinafter, and as presented before, we refer to the doped compound as $La_{2-x}Sr_xCuO_4$, though a quantitative analysis on the exact value of both T and x is not our concern. Instead, we shall present a brief and qualitative analysis of how T and x determine the phases of our system.

Let us start with the undoped case. First, note that since La has oxidation state +3 and O has -2 , chemical composition of our compound brings us to conclude that the Cu presents oxidation state +2, thus having a $3d^9$ electronic configuration. From this fact, one might naively expect the La_2CuO_4 to be a metal. However, it comes out to be an antiferromagnetic insulator (see Figure 1.7). Therefore, rather than basing our understanding only upon simple chemical arguments, it is essential to consider electron-electron correlation. At $x = 0$, and as commonly known for a

generic antiferromagnetic material, rising the temperature will eventually lead to a phase transition, becoming a metallic conductor after reaching the Néel temperature T_N .

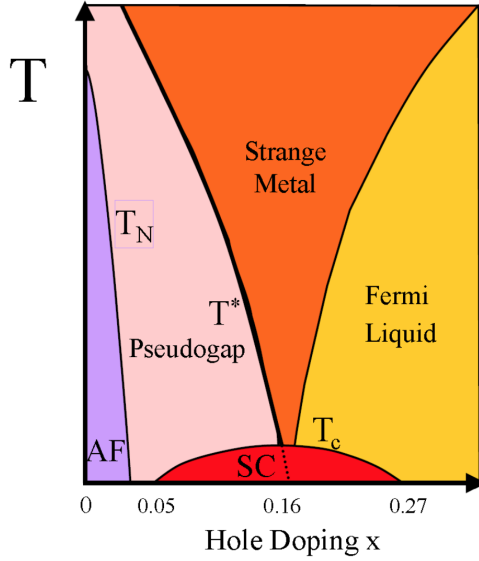


Figure 1.7: High T_c temperature-doping phase diagram AF and SC stand for antiferromagnetic and superconductor, respectively. T_N denotes the Néel temperature. Reference: [6].

This temperature is found to be about $T = 325$ K [9]. We shall remark that this is not just a Néel transition. In fact, there is a simultaneous magnetic and electronic transition (from AFM to paramagnetic and from insulator to metal).

When La_2CuO_4 is doped, several transitions take place. This doping considerably reduces T_N , as depicted in Figure 1.7. Above $x \sim 0.02$, long-range magnetic order is destroyed, though there are still some short-range interactions. At this point, the system behaves as a 2D disordered metal and it has entered the so called “**pseudogap**” region. The term pseudogap refers to a state whose Fermi surface has a partial or incomplete energy gap. This phenomenon is quite similar to a true energy gap, but in our case there are some - though very few - states within this gap region.

Moreover, exotic hole orderings in the form of vertical and diagonal **stripes** can be found in this region (for more detail, cf. [12]).

At about $x = 0.05$ superconductivity appears, reaching a maximum for $T_c \sim 40$ K at $x \sim 0.16$ (called “optimal doping”) and again decreasing for overdoped states. Above this maximum at optimal doping we find a wedge-shape strange metal region characterized by a linear dependence of resistivity with temperature. If we increase even more the doping, the systems enters a region called Fermi liquid region, where it can be properly explained by the homonymous theory.

1.3 Objectives of this work

This works aims to create a simple model that gives some insight on the Physics of part of the phase diagram (Figure 1.7). In particular, we will focus on what happens at $x = 0$ (no doping) when temperature increases, coming across a simultaneous magnetic and insulator-metal transition. This is also a tough computational challenge as DFT-based methods are usually not prepared to deal with temperature. In more detail, we shall

- i) Find out a way to relate our system’s total energy and its magnetic ordering, determining their dependency. This allows us to verify that our ground state is indeed antiferromagnetic while at the same we may keep track of the system’s magnetic state in a simple way.
- ii) Perform a temperature-based simulation by means of a Markov Chain Monte Carlo (MCMC) method in order to reproduce the sought phase transition.

This model considers two-dimensional systems, aiming to describe the CuO_2 layers of La_2CuO_4 .

The validation of this simple model is important beyond the goals of this work, as it could be easily expanded to describe other regions of the temperature-doping phase diagram. For example, experimental data from X-ray absorption spectroscopies [13] confirm that holes lay on the CuO_2 planes. Therefore, explaining how this system behaves with doping might be done by just generalizing our model.

1.4 Structure of this work

After having introduced the problem of superconductivity and the system we shall deal with, goal of the next chapter is to give a thorough look at the computational methods used in this work. We shall set up the ideas of a DFT-based second-principles simulation and how these techniques can be adapted to our particular problem. Complementary to this, the chapter describes the tools that allow us to take temperature into account for our analysis.

The third chapter contains the main results of our work, presenting one by one the elements that allow us to fully describe and understand the chosen system within our model's framework. By the end of this chapter, the reader will be able to witness how all these elements combined reproduce the sought magnetic and insulator-metal transition.

Finally, the last chapter consists of a brief summary of our achievements and to what extent this work might be extended beyond its scope.

Chapter 2

Computational methods

In Quantum Mechanics, and in particular in Solid State Physics, solving the time-independent Schrödinger equation is necessary to understand and predict the state of any system and the properties associated with it. However, handling this problem is in general difficult, due to the fact that the wave function we are looking for depends on the position of a large number of electrons.

Throughout the last few decades, the fast development of computational techniques has allowed us to solve the Schrödinger equation from first-principles (*ab initio*), that is, without the need to use any kind of experimental input data. Hence, the computational methods have become an essential tool for us to thoroughly understand the nature of complex quantum systems, turning out to be an important complementary approach to that of the experiments.

In this chapter, our aim is to introduce and present the foundations of the first-principles techniques, the approximations they are based on and their limitations. More concretely, we shall devote our attention to the Density Functional Theory (abbreviated DFT), focusing on the Kohn-Sham approach. We will conclude this overview of the computational methods with a description of the DFT-based second-principles techniques (SP-DFT) implemented in the code SCALE-UP, arguing their suitability for the problem of La_2CuO_4 we are dealing with in this work. Afterwards, we will briefly delve ourselves into the foundations of the tight-binding model and the Hubbard model and how they may be expressed in terms of the SP-DFT formalism, discussing why those turn out to be suitable for the goal we are pursuing in this project. Finally, we will introduce a Markov Chain Monte Carlo method and its usefulness in the context of the study of magnetic systems; providing a tool to predict temperature behaviour and search for phase transitions.

Contents

2.1	First principles methods	12
2.1.1	Notation	12
2.1.2	Hamiltonian	12
2.1.3	Adiabatic approximation	13
2.1.4	Electronic hamiltonian	14
2.1.4.1	Hartree-Fock method	14
2.1.4.2	DFT	17
2.1.4.2.1	Hohenberg-Kohn Theorems	17
2.1.4.2.2	Kohn-Sham approach	18
2.2	Second-principles methods	20
2.2.1	Overview of SP-DFT	21

2.2.2	Energy in SP-DFT	21
2.3	Effective form of the SP Hamiltonian in this work	22
2.3.1	Tight-binding model	22
2.3.2	Two-electron interactions: Hubbard model	23
2.4	Monte Carlo method and implementation in this work	25

2.1 First principles methods

2.1.1 Notation

In the following, we consider a quantum mechanical system which is composed of N electrons and M nuclei. We denote the nuclei positions by capital letters \vec{R}_α and those of the electrons with a lower-case \vec{r}_i . In order to refer to the nuclei we adopt the convention of using Greek alphabet letters (α, β, γ , etc.), whereas the electrons are labeled with Latin alphabet symbols (a, b, c , etc.). Therefore, we might write the complete set of nuclei (resp. electrons) as $\{\vec{R}\} = \{\vec{R}_\alpha, \vec{R}_\beta, \vec{R}_\gamma, \dots\}$ (resp. $\{\vec{r}\} = \{\vec{r}_a, \vec{r}_b, \vec{r}_c, \dots\}$).

For the sake of simplicity and whenever necessary, we assume a periodic three dimensional infinite crystal, with lattice cells denoted by upper-case letters (Λ, Δ, \dots) and the atoms in the cell by lower-case letters (λ, δ, \dots). For example, the lattice vector of cell Λ is \vec{R}_Λ , whilst the reference position of the atom might be written as \vec{R}_λ , i.e., with a lower-case bold subindex.

2.1.2 Hamiltonian

In Solid State Physics, we devote ourselves to the study of quantum mechanical systems that add up to macroscopic crystalline solids. The formulation of the problem is quite generic and might seem trouble-free: obtaining the global wave function $|\Psi\rangle$ that describes the whole system, thus containing its entire information. In order to obtain this wave function, we shall solve the Schrödinger equation:

$$\hat{\mathcal{H}}(\{\vec{R}\}, \{\vec{r}\}, t) |\Psi(\{\vec{R}\}, \{\vec{r}\}, t)\rangle = i\hbar \frac{\partial}{\partial t} |\Psi(\{\vec{R}\}, \{\vec{r}\}, t)\rangle, \quad (2.1)$$

where \hbar is the reduced Planck constant and $\hat{\mathcal{H}}$ is the hamiltonian. All the information regarding interactions among particles in the considered system is contained in this term. Hereafter, for our purpose, we consider a purely electrostatic hamiltonian.

This hamiltonian contains the kinetic contributions of both electrons (\hat{T}_e) and nuclei (\hat{T}_n), as well as electrostatic interactions between nuclei (\hat{V}_{nn}), electrons (\hat{V}_{ee}) and nuclei and electrons (\hat{V}_{en}). In the case that there is some external potential, an additional term (\hat{V}_{ext}) comes into the hamiltonian. Summarizing, we may write a non-relativistic hamiltonian as follows:

$$\hat{\mathcal{H}} = \hat{T}_e + \hat{T}_n + \hat{V}_{nn} + \hat{V}_{ee} + \hat{V}_{en} + \hat{V}_{ext}. \quad (2.2)$$

The kinetic energy terms are written in terms of the square of the linear momentum for each of the constituents, in our case:

$$\hat{T}_e = \sum_{a=1}^N \frac{\hat{p}_a^2}{2m_a} = -\hbar^2 \sum_{a=1}^N \frac{\nabla_a^2}{2m_a} \quad ; \quad \hat{T}_n = \sum_{\alpha=1}^M \frac{\hat{p}_\alpha^2}{2M_\alpha} = -\hbar^2 \sum_{\alpha=1}^M \frac{\nabla_\alpha^2}{2M_\alpha}. \quad (2.3)$$

The expression for the electrostatic interactions has a classical resemblance as well. Written in atomic units:

$$\hat{V}_{ee} = \sum_{a=1}^N \sum_{b>a}^N \frac{1}{|\vec{r}_a - \vec{r}_b|} \quad ; \quad \hat{V}_{nn} = \sum_{\alpha=1}^M \sum_{\beta>\alpha}^M \frac{Z_\alpha Z_\beta}{|\vec{R}_\alpha - \vec{R}_\beta|} \quad ; \quad \hat{V}_{en} = \sum_{a=1}^N \sum_{\alpha=1}^M \frac{Z_\alpha}{|\vec{r}_a - \vec{R}_\alpha|}. \quad (2.4)$$

These last equations are the reason behind the enormous complexity of the Schrödinger equation: the cross terms that arise in the electrostatic interactions hinder finding an exact and analytical resolution of Eq. (2.1), just as for any equation of relative motion that involves two or more bodies [14]. We define the electronic hamiltonian as follows:

$$\hat{\mathcal{H}}_{el} = \hat{T}_e + \hat{V}_{nn} + \hat{V}_{ee} + \hat{V}_{en} + \hat{V}_{ext}. \quad (2.5)$$

Hence, the total hamiltonian defined in Eq. (2.2) is more appropriately studied when considered as a sum of $\hat{\mathcal{H}}_{el}$ and the kinetic energy of the nuclei.

Moreover, if there is no time dependence in the hamiltonian, for the A-th stationary state of the system we may rewrite the total wave function $|\Psi\rangle$ as a product of a time-dependent part $|\Theta_A(t)\rangle$ and a space-dependent part $|\Psi_A(\{\vec{R}\}, \{\vec{r}\})\rangle$ [14]. Whereas the solution for $|\Theta_A(t)\rangle$ is trivial, that of $|\Psi_A(\{\vec{R}\}, \{\vec{r}\})\rangle$ corresponds to the time independent Schrödinger equation:

$$\hat{\mathcal{H}}(\{\vec{R}\}, \{\vec{r}\})|\Psi_A(\{\vec{R}\}, \{\vec{r}\})\rangle = E_A|\Psi_A(\{\vec{R}\}, \{\vec{r}\})\rangle. \quad (2.6)$$

This equation provides the stationary states Ψ_A of the system, those with a constant electronic density and each with a different energy. It is clear that dealing with Eq. (2.6) is in fact quite complicated due to the presence of cross terms hinder any analytical solution. That is the reason why we must adopt crucial approximations that make the resolution of the Schrödinger equation slightly more handleable. Two of the most important are the adiabatic approximation and the independent electron approximation.

2.1.3 Adiabatic approximation

One of the (many) possible adiabatic approximations is that of Born-Oppenheimer. Briefly speaking, this approach is based on the fact that nuclei are much heavier than electrons and thus their motion may be treated separately [14]. Let us see in detail the foundations of this approach, which acts in two consecutive steps.

(I) Dynamic of electrons with fixed nuclei: Compared with electrons, nuclei have large masses and therefore in general (due to the equipartition theorem), small velocities. The first step consists in studying the motion of electrons with fixed nuclei. In other words, the nuclei positions \vec{R}_α may be considered to be fixed parameters. The equation in eigenvalues for the corresponding electronic hamiltonian is

$$\hat{\mathcal{H}}|\Psi_A(\{\vec{R}\}, \{\vec{r}\})\rangle = E_A(\{\vec{R}\})|\Psi_A(\{\vec{R}\}, \{\vec{r}\})\rangle. \quad (2.7)$$

This equation can be solved for fixed values of $\{\vec{R}\}$, obtaining the electronic states A corresponding to wave functions $\Phi_A(\{\vec{R}\}, \{\vec{r}\})$ and energies $E_A(\{\vec{R}\})$. Repeating this process for multiple sets $\{\vec{R}\}$ of nuclei positions, we end up with an energy equipotential surface $E_A(\{\vec{R}\})$ for each electronic state A, usually known as *Potential Energy Surface (or APES)*

Note that $\{|\Phi_A(\{\vec{R}\}, \{\vec{r}\})\rangle\}$ is an orthonormal complete set of electronic wave functions. Consequently, every function, in particular the exact total wave functions $|\Psi(\{\vec{R}\}, \{\vec{r}\})\rangle$, may be written as an exact series of the electronic wave functions:

$$|\Psi(\{\vec{R}\}, \{\vec{r}\})\rangle = \sum_{A=1}^{\infty} |\Omega_A(\{\vec{R}\})\rangle |\Phi_A(\{\vec{R}\}, \{\vec{r}\})\rangle, \quad (2.8)$$

where the coefficients $|\Omega_A(\{\vec{R}\})\rangle$ depend on the values $(\{\vec{R}\})$ because the nuclei positions are indeed variables in the total wave function $|\Psi(\{\vec{R}\}, \{\vec{r}\})\rangle$.

(II) Nuclei motion under the potential created by the electrons: Furthermore, the adiabatic approximation states that the effect of the nuclear momentum operator \hat{T}_n on the electron's wave function may be neglected, i.e., $\hat{T}_n\Phi_A(\{\vec{R}\}, \{\vec{r}\}) \approx 0$. Thus, simplifying notation, taking $|\Psi\rangle$ as in Eq. (2.8) and multiplying in Eq. (2.7) by the bra $\langle\Phi_B|$, we obtain

$$\left[\hat{T}_n + E_A(\{\vec{R}\})\right] |\Omega_A(\{\vec{R}\})\rangle = E |\Omega_A(\{\vec{R}\})\rangle. \quad (2.9)$$

Eq. (2.9) has the form of a Schrödinger equation for the movement of the nuclei under a potential which is exactly the APES $E_A(\{\vec{R}\})$ corresponding to the electronic state A .

2.1.4 Electronic hamiltonian

Once that we have introduced the adiabatic approximation, and consequently decoupled electrons' dynamics from that of nuclei, we shall solve the Schrödinger equation for the electronic hamiltonian (equation (2.7)). As anticipated, the dynamics of a many-electron system is quite complex as we still have to deal with electron-electron repulsion terms of the form $\frac{1}{|\vec{r}_a - \vec{r}_b|}$. A remarkable simplification though may be achieved by considering the whole electrons' interaction as an average, and thus describing the motion of the N electrons *as if* they were under a mean potential, or mean field.

For a system composed of N electrons, the idea of the independent electron approximation consists in considering the total wave function of a system for a certain state as a combination of N independent wave functions properly chosen. Let $\tilde{\Psi}$ be the approximate total wave function of our system, Ψ be the exact one and E its exact energy. From the variational principle (see [14, p.570-571]), we may show that

$$\tilde{E} = \langle\tilde{\Psi} | \hat{H}_{el} | \tilde{\Psi}\rangle \geq \langle\Psi | \hat{H}_{el} | \Psi\rangle = E. \quad (2.10)$$

That is, the energy of every approximate solution is always larger than that of the exact one. The idea of these methods is to minimize the energy \tilde{E} until reaching a minimum, which should be theoretically the exact energy we are pursuing.

2.1.4.1 Hartree-Fock method

In 1927, the English physicist D.R. Hartree introduced what he called a self-consistent field method to calculate approximate wave functions for systems with multiple particles. His idea, which was indeed the first example of an independent electron approximation, consisted in writing the total wave function as a product of one-electron wave functions (orbitals):

$$\tilde{\Psi}(r_1, \dots, r_N) = \psi_1(\vec{r}_1) \dots \psi_N(\vec{r}_N). \quad (2.11)$$

The main problem under this approach is that the product in (2.11) does not satisfy the Pauli exclusion principle, which states that the total wave functions describing fermionic systems must be antisymmetric with respect to the exchange of two arbitrary particles. This issue was overcome by the Russian physicist W. Fock, who proposed in 1930 a wave function given as the product of a spatial orbital and a spin function. In a general case, assuming N electrons and N spin-orbitals, we may express our wave function as a *Slater determinant*, defined as:

$$\tilde{\Psi}(\vec{r}_1, \dots, \vec{r}_N) = \frac{1}{\sqrt{N!}} \begin{vmatrix} \psi_1(\vec{r}_1) & \psi_2(\vec{r}_1) & \dots & \psi_N(\vec{r}_1) \\ \psi_1(\vec{r}_2) & \psi_2(\vec{r}_2) & \dots & \psi_N(\vec{r}_2) \\ \vdots & \vdots & \ddots & \vdots \\ \psi_1(\vec{r}_N) & \psi_2(\vec{r}_N) & \dots & \psi_N(\vec{r}_N) \end{vmatrix} ; \quad \langle \psi_i | \psi_j \rangle = \delta_{ij}. \quad (2.12)$$

Each of the terms that appear in the determinant is written as a product of a spatial function ϕ_i and a spin function χ_i , so that $\psi_i = \phi_i \chi_i$. The most drastic approximation is to take one single Slater determinant.

Having chosen a single Slater determinant as a test function, the next step uses the Rayleigh-Ritz variational principle to find the optimal ψ_i that minimizes the energy. It shall be remarked that during this process, the approximate wave function $\tilde{\Psi}$ must be introduced into the Schrödinger equation with the exact electronic hamiltonian. After some calculation, which can be found in detail in [14, p. 88-93], this procedure leads to the Hartree-Fock (HF) equations:

$$\left[-\frac{\hbar}{2m} \nabla_a^2 + \sum_{\alpha} \frac{Z_{\alpha}}{|\vec{r} - \vec{R}_{\alpha}|} + \hat{J}_a - \hat{K}_a \right] \psi_a = \varepsilon_a \psi_a \quad a = 1, \dots, N. \quad (2.13)$$

Let us see in detail the terms appearing in (2.13). The operator \hat{J} stands for the classical Coulomb electron-electron repulsion, whereas the operator \hat{K} represents the exchange interaction, arisen from the Pauli exclusion principle and without classical analogous. Acting on wave functions:

$$\hat{J}_a | \psi_b \rangle = \left(\int |\psi_b|^2 \frac{1}{|\vec{r}_a - \vec{r}_b|} d\vec{r}_b^3 \right) | \psi_b \rangle, \quad (2.14)$$

$$\hat{K}_a | \psi_b \rangle = \left(\int \psi_a^* \psi_b \frac{1}{|\vec{r}_a - \vec{r}_b|} d\vec{r}_b^3 \right) | \psi_a \rangle. \quad (2.15)$$

Setting $J_{ab} := \langle \psi_b | \hat{J}_a | \psi_b \rangle$ and $K_{ab} := \langle \psi_b | \hat{K}_a | \psi_b \rangle$, the set of coupled HF equations in Eq. (2.13) leads to the following ground state energy [14]:

$$E_{HF} = \sum_{i=1}^N h_a + \frac{1}{2} \sum_{a,b=1}^N (J_{ab} - K_{ab}) + V_{nn} \quad ; \quad h_a = \left\langle \psi_a \left| \hat{h}_a \right| \psi_b \right\rangle, \quad (2.16)$$

where \hat{h}_i takes into account the motion of the i -th electron under the field created by the nuclei:

$$\hat{h}_a = -\frac{1}{2} \nabla_a^2 - \sum_{A=1}^M \frac{Z_A}{|\vec{R}_A - \vec{r}_a|}. \quad (2.17)$$

We may see the following [16]:

- i) $K_{aa} = J_{aa}$, and consequently the Coulomb interaction of one electron with itself vanishes with the exchange interaction term K_{aa} .
- ii) For the exchange interaction it holds $K_{ab} \propto \delta_{m_{sa}, m_{sb}}$, where m_{sa} stands for the spin's third component of the electronic state a . Therefore, antiparallel spins lead to $K_{ab} = 0$.
- iii) For electrons with the same spin, the integrals K_{ab} are always positive, reducing the Coulomb repulsions J_{ab} . This fact can be understood as if in a neighbourhood of each electron there were an absence of charge of the same spin (Fermi hole), preventing that electrons of same spin get close to each other.

As already mentioned, in this procedure we are assuming that the repulsion between an electron and all the others may be described by a set of orbitals. The electron-electron repulsion is only taken into account as an average, and that is why the HF method might be referred as a *mean-field* approximation.

We may write the expression for the HF equations in Eq. (2.13) in a more compact way by defining the *Fock operator* for each orbital ψ_a :

$$\hat{F}_a := \hat{h}_a + \sum_{b=1}^N (\hat{J}_b - \hat{K}_b). \quad (2.18)$$

And hence the HF equations take the form

$$\hat{F}_a \psi_a = \varepsilon_a \psi_a \quad a = 1, \dots, N. \quad (2.19)$$

If a family of orbitals satisfies the former expressions for the Fock operator, we say that they are a *self-consistent field (SCF)* set. Analogously, the procedure to find out the orbitals is called iterative self-consistent method:

- i) We start by making a rough estimation of the orbitals ψ_a .
- ii) Solve equation (2.19) for each orbital.
- iii) Determine whether the orbitals obtained in the last step differ from the formers. If so, repeat from *ii*).

This process ends when the difference between orbitals lies under a previously defined SCF threshold.

Besides this, it is important to remark that the Hartree-Fock energy written in (2.16) corresponds to that of a concrete configuration, that is, a single Slater determinant. Further improvement of the energy also based on multielectronic wave functions may be achieved by considering an expansion of the system's wave functions whose terms are Slater determinants for configurations different from that of the ground state (that is, excited configurations):

$$\Psi = \sum_i \alpha_i \tilde{\Psi}_i \quad (2.20)$$

Since the obtained energy is not the exact one, the term *correlation energy* is coined to denote the difference between E_{HF} and the actual energy.

The main problem of the HF algorithms, and one of the reasons why they are not pretty much used anymore, is because of their high computational cost. This is due to the $\mathcal{O}(N^5)$ complexity that the computation of K_{ab} and J_{ab} presents. Moreover, if we explicitly take correlation into account, this complexity scales to $\mathcal{O}(N^7)$, $\mathcal{O}(N^9)$, etc. One alternative to HF is the so called *density functional theory*, better known as *DFT*, with a much smaller computational complexity of $\mathcal{O}(N^3)$.

2.1.4.2 DFT

As already mentioned in previous sections, HF and post-HF are complex from a computational point of view. The Density Function Theory (DFT) offers a cheaper alternative to solve the Schrödinger

equation. Whereas in HF methods approximations are made on wave functions, DFT only takes the electronic density into account:

$$\rho(\vec{r}) = \int |\Psi(\vec{r}_1, \dots, \vec{r}_N)|^2 d\vec{r}_1 \dots d\vec{r}_N. \quad (2.21)$$

Hereinafter, the energy of the system may be written as a functional of the electronic density, which only depends on three spacial variables, no matter how many particles our system has. This is a remarkable breakthrough compared to methods that deal with wave functions and approximations on them, for which the complexity increases exponentially with the number of electrons.

There is though a mathematical abstraction underneath. When we talk about a *function*, we refer to a correspondence that produces a number from another number or a set of variables (mainly coordinates). The term *functional* owes its origin to the Functional Analysis, and more concretely to the concept of dual space of an arbitrary vector space V over a field \mathbb{K} :

$$V^* := \{L : V \rightarrow \mathbb{K} : L \text{ is linear and continuous}\}. \quad (2.22)$$

That is, the set of all continuous homomorphisms from a vector space to its field. In our case, we simply denote a correspondence *functional* if it produces a number from a function. This is precisely the case when V is a vector space made of functions (for example the $L^p(\mathbb{R})$ spaces). We will denote a function as usual, $f(x)$, whereas a functional may be properly written with brackets, namely $F[f]$.

We are hence pursuing the energy as a functional of the electronic density, i.e., $E[\rho]$. It is straightforward to see that the energy functional may be split into three parts [14]: kinetic energy $T[\rho]$, electrons-nuclei attraction $V_{en}[\rho]$ and electron-electron repulsion $V_{ee}[\rho]$. At the same time, and similarly to the HF approach, we may divide $V_{ee}[\rho]$ into the Coulomb repulsion $J[\rho]$ and the exchange interaction $K[\rho]$. The expression for $V_{en}[\rho]$ and $J[\rho]$ is the classical one [14],

$$V_{en}[\rho] = - \sum_{A=1}^N \int \frac{Z_A}{|\vec{R}_A - \vec{r}|} \rho(\vec{r}) d\vec{r} \quad ; \quad J[\rho] = \frac{1}{2} \int \int \frac{\rho(\vec{r})\rho(\vec{r}')}{|\vec{r} - \vec{r}'|} d\vec{r} d\vec{r}'. \quad (2.23)$$

This approach was firstly introduced in the 1920's. Though attractive, it did not reproduce electronic energies just as wavefunctions do [17]. It was not until the 1960's when it experienced a "Reinassance" thanks to the contributions of Hohenberg and Kohn, who established the foundations of the modern DFT by means of their two known theorems. Roughly speaking, this theory relies on the fact that the ground state energy is fully determined by the electronic density ρ .

2.1.4.2.1 Hohenberg-Kohn Theorems

DFT is based upon the following two results [18]:

Theorem 2.1. *For the ground state of any system, the external potential $v_{ext}(\vec{r})$ is uniquely determined, up to an additive constant, by its electronic density $\rho(\vec{r})$.*

There is a reciprocal for the previous theorem:

Corollary 2.2. *The electronic density $\rho(\vec{r})$ of the ground state is uniquely determined by the external potential $v_{ext}(\vec{r})$.*

Proof. This result is trivial because the external potential $v_{ext}(\vec{r})$ determines the Hamiltonian from which the wave function is extracted and thus the electronic density by means of the definition in eq. (2.21). \square

The main conclusion that we may draw from the previous results is that if we know either the electronic density or the external potential, the other one is fully determined.

We shall remark that the term “external potential” in this context refers to any interaction involving the electrons that does not arise from them. Therefore, we must include the electron-electron repulsion V_{ee} , the electron-nucleus attraction V_{en} , and the term V_{ext} that appeared in the electronic hamiltonian defined in (2.5). Hence,

$$\hat{v}_{ext} = \hat{V}_{en} + \hat{V}_{ext}. \quad (2.24)$$

From Theorem 2.1, we know that ρ and v_{ext} are uniquely connected with each other, though we do not know how. The second theorem of Hohenberg-Kohn establishes a relationship between the ground state electronic density and the external potential:

Theorem 2.3. *Let $\tilde{\rho}(\vec{r})$ be a trial ground state density such that $\tilde{\rho}(\vec{r}) \geq 0$ and*

$$\int \tilde{\rho}(\vec{r}) d\vec{r} = N.$$

Then, it holds that $E \leq E_v[\tilde{\rho}(\vec{r})]$, where $E_v[\tilde{\rho}(\vec{r})]$ is a trial energy functional for E corresponding to an external potential v and E is the exact ground state energy.

This theorem states that every functional for the energy written in terms of the electronic density reaches a global minimum which corresponds to the actual value of the energy.

The first problem that arises is that ρ is unknown. However, we do know how the electronic density interacts with an external potential, so we may write the following functional for the energy:

$$E[\rho] = F_{HK}[\rho] + \int \rho(\vec{r}) v_{ext}(\vec{r}) d\vec{r}, \quad (2.25)$$

where $F_{HK}[\rho]$ represents an universal functional of the density valid for every system [18]. It shall contain the kinetic energy of the electrons and the interaction among themselves.

Summing up, the second Theorem of Hohenberg-Kohn conceives the DFT as a variational method to compute the ground state by optimizing the functional of the density for the energy.

2.1.4.2.2 Kohn-Sham approach

Although the previous theorems establish a solid theoretical foundation of the DFT methods, we still do not know the expression of the $F_{HK}[\rho]$ functional. Kohn and Sham [19] suggested in 1965 a breakthrough idea that allowed the DFT formulation to become one of the most successful approaches nowadays to investigate the electronic structure of many bodies system.

Their idea consists in substituting the actual system by a fictitious one made of N non-interacting fermions described by a set of orbitals $\{\phi_i\}_{i=1}^N$ under an average potential v_{ext} . The system that we have just made up shall present the same electronic density and energy for the ground state as the real one. This independent-electron approach reminds us of the HF methods, and in fact the KS model is closely related to it, sharing similar formulas for the kinetic, electron-nuclear and electron-electron energies [14].

Let us commence by noting that our system’s kinetic energy may be described *exactly*, since we are handling N non-interacting electrons. Thus, we write

$$T_S = \sum_{i=1}^N \left\langle \phi_i \left| -\frac{1}{2} \nabla^2 \right| \phi_i \right\rangle, \quad (2.26)$$

where the S sub-index denotes that the energy is calculated from a Slater determinant. The proposal of Kohn and Sham for F_{HK} relies on the following decomposition:

$$F_{HK}[\rho] \equiv T_S[\rho] + J[\rho] + E_{xc}[\rho]. \quad (2.27)$$

Here, $J[\rho]$ denotes the Coulomb repulsion, defined in eq. (2.23). The term $E_{xc}[\rho]$, defined as [14]:

$$E_{xc}([\rho]) = (T[\rho] - T_S[\rho]) + (V_{ee}[\rho] - J[\rho]). \quad (2.28)$$

This unknown functional - called exchange-correlation functional - contains within its first parenthesis a correction to the the kinetic energy (i.e., the difference between the real and the non-interacting kinetic energy), which we expect to be a small number. The last parenthesis contains the difference between the full electron-electron interaction and the classical Coulomb interaction, which should be small as well. With reference to Hartree-Fock theory (eq. (2.16)), the term $V_{ee}[\rho]$ may be divided into a Coulomb and an exchange part, $J[\rho]$ and $K[\rho]$, so the second parenthesis implicitly includes the exchange and correlation energies [14].

The key idea here is to calculate the kinetic energy under the assumption of non-interacting electrons. As we may expect, the electrons are actually interacting, though baring in mind that HK theory predicts approximately 99% of the correct answer for the kinetic energy, this approximation is not that drastic [14].

Substituting Eq. (2.27) in Eq. (2.25), we obtain

$$E[\rho] = T_S[\rho] + J[\rho] + E_{xc}[\rho] + \int \rho(\vec{r}) v_{ext}(\vec{r}) d\vec{r}. \quad (2.29)$$

We now must delve into finding out an expression for $E_{xc}[\rho]$, which remains unknown. First, recall that our *made-up* system has the same density as the real one, so we can write $\rho(\vec{r})$ in terms of the set of orbitals $\{\phi_i\}_{i=1}^N$ and the respective occupation n_i :

$$\rho(\vec{r}) = \sum_{i=1}^N n_i |\phi_i(\vec{r})|^2. \quad (2.30)$$

Similarly to HF, we may apply the variational principle on Eq. (2.29) (second HK theorem), which leads us to the so called Kohn-Sham equations:

$$\hat{h}_s \phi_i = \left[-\frac{1}{2} \nabla^2 + v_{eff} \right] \phi_i = \epsilon \phi_i, \quad i = 1, \dots, N. \quad (2.31)$$

This set of equations is analogous to that of our fictitious system (which would be Hartree-Fock-like) except for the presence of an effective potential:

$$v_{eff}(\vec{r}) = v_{ext}(\vec{r}) + \underbrace{\frac{\delta J[\rho]}{\delta \rho(\vec{r})}}_{-v_H(\vec{r})} + \underbrace{\frac{\delta E_{xc}[\rho]}{\delta \rho(\vec{r})}}_{v_{xc}(\vec{r})}. \quad (2.32)$$

The second and the third terms are called Hartree potential (behold the minus sign) and exchange correlation potential, respectively. Consequently, we can write the total DFT energy as follows [20]:

$$E_{DFT} = \sum_{i=1}^N n_i \left\langle \phi_i \left| -\frac{1}{2} \nabla^2 + v_{ext} \right| \phi_i \right\rangle + \frac{1}{2} \int \int \frac{\rho(\vec{r}) \rho(\vec{r}')}{|\vec{r} - \vec{r}'|} d\vec{r} d\vec{r}' + E_{xc}[\rho] + E_{nn}. \quad (2.33)$$

Note that the first term of the previous expression includes the kinetic energy of a system of non-interacting electrons under the action of an external potential that contains contributions from nuclei and, if so, other external fields. The second term refers to the Coulomb electrostatic energy, the third is the exchange correlation energy (as previously defined) and the fourth stands for the nucleus-nucleus interaction.

In conclusion, the DFT techniques seek to improve an expression for $E_{exc}[\rho]$ in order to determine the energy of the system as accurately as possible. Some of the approximations for this aim are the *Local Density Approximation (LDA)*, which derives the exchange correlation functional from that of an homogeneous electron gas using Monte Carlo techniques, and the *Generalized Gradient Approximation (GGA)*, which also takes into account the density's gradient [?, ?]. However, first-principles methods, even with this approach, result in high computational costs that do not allow us to handle a large number of particles (usually beyond 1000 atoms). This is precisely the reason why we must introduce the so-called Second Principles methods.

Even so, we shall note that using DFT has other limitations. In particular, DFT works at zero temperature. This fact constrains our work to very ordered systems, justifying the use of a Monte Carlo method that will be introduced in section 2.4.

2.2 Second-principles methods

As already anticipated, first-principles techniques have a quite solid theoretical foundation that allows us to solve the Schrödinger equation, and thus study electronic properties of physical systems accurately. Nevertheless, the greatest limitation of this approach is based on its high computational cost, not to mention how unmanageable it becomes to deal with a large number of particles. In particular, this work aims to study magnetic properties of bidimensional systems that can only be properly observed if we consider a sufficiently large lattice. The presence of a global magnetic ordering (ferromagnetic or antiferromagnetic), together with all the intermediate states (characterized by a distribution of magnetic domains that appear gradually as we increase the temperature) may be neglected if the lattice is not big enough.

In order to overcome these limitations, several techniques have been recently developed. Among them, we are going to focus on the so called second-principles DFT (SP-DFT) approach, and later on we will discuss its validity within this work's object of study.

The main restriction of this theory relies on the assumption that there is an underlying lattice or bonding topology which is preserved along the simulation. This premise allows us to systematically improve the accuracy of classical DFT calculations. Hereinafter, and unless otherwise indicated, we will follow [20].

2.2.1 Overview of SP-DFT

As usually done in most first-principles schemes, we assume the validity of the Born-Oppenheimer (or adiabatic) approximation, that allows us to consider electrons and nuclei motion separately. For the forthcoming overview we shall deal with two new concepts: the *reference atomic geometry (RAG)* and the *textitreference electronic density (RED)*. First, we shall make a choice of a RAG, i.e., a particular configuration of the nuclei used as reference for any other configuration. This RAG is usually taken to be the ground state or, failing that, a high symmetrical configuration.

The second step is the election of a RED - which we call $\rho_0(\vec{r})$ in order to be consistent with the previous notation - for each possible atomic configuration. The validity of our model is based on the fact that the actual electronic density, $\rho(\vec{r})$, will be very closed to the RED. Hence, we may describe changes in physical properties in terms of a (small compared to $\rho_0(\vec{r})$) deformation density $\delta\rho(\vec{r})$ as follows:

$$\rho(\vec{r}) = \rho_0(\vec{r}) + \delta\rho(\vec{r}). \quad (2.34)$$

2.2.2 Energy in SP-DFT

We seek to find a functional that yields an accurate expression of the DFT energy (see Eq. (2.33)). The greatest issue we have to overcome is the exchange correlation energy $E_{xc}[\rho]$ in that expression which, additionally, is not linear with respect to the electronic density. However, the assumption that the perturbation density $\delta\rho(\vec{r})$ is small compared to the reference density $\rho_0(\vec{r})$ permits us to consider a Taylor series of $E_{xc}[\rho]$ near ρ_0 as follows:

$$E_{xc}[\rho] = E_{xc}[\rho_0] + \int \frac{\delta E_{xc}}{\delta\rho(\vec{r})} \Big|_{\rho_0} \delta\rho(\vec{r}) d\vec{r} + \frac{1}{2} \int \int \frac{\delta^2 E_{xc}}{\delta\rho(\vec{r})\delta\rho(\vec{r}')} \Big|_{\rho_0} \delta\rho(\vec{r})\delta\rho(\vec{r}') d\vec{r}d\vec{r}' + \dots \quad (2.35)$$

Recall that the terms inside of the integrals correspond to functional derivatives of E_{xc} . This approach permits us to write the total energy as a perturbative sum of terms coming from different contributions of the deformation density (with respect to the reference density)

$$E_{DFT} \approx E = E^{(0)} + E^{(1)} + E^{(2)} + \dots \quad (2.36)$$

$E^{(0)}$, also called zeroth term, corresponds to the DFT energy associated with the ground state energy, provided with a non-perturbed electronic density $\rho_0(\vec{r})$. Hence, this energy term obeys the expression (2.33) but with $\rho_0(\vec{r})$ instead of the real density $\rho(\vec{r})$. Cheap computation of $E^{(0)}$ may be performed by using a model potential that only depends on the atomic positions where electrons are integrated out, thus being a huge advantage with respect to classical DFT methods that require an explicit treatment to tackle electronic interactions [20].

The first order term $E^{(1)}$ involves one-electron interactions:

$$E^{(1)} = \sum_{i=1}^N \left[n_i \langle \phi_i | \hat{h}_0 | \phi_i \rangle - n_i^{(0)} \langle \phi_i^{(0)} | \hat{h}_0 | \phi_i^{(0)} \rangle \right], \quad (2.37)$$

where \hat{h}_0 denotes the Kohn-Sham hamiltonian as defined in the equation (2.31) but for the reference density $\rho_0(\vec{r})$, that is:

$$\hat{h}_0 = -\frac{1}{2}\nabla^2 + v_{eff}^{(0)} = -\frac{1}{2}\nabla^2 + v_{ext} - v_H[\rho_0; \vec{r}] + v_{exc}[\rho_0; \vec{r}]. \quad (2.38)$$

Finally, the second term $E^{(2)}$, also called two-electron energy, is given by

$$E^{(2)} = \frac{1}{2} \int d\vec{r} \int d\vec{r}' g(\vec{r}, \vec{r}') \delta\rho(\vec{r}) \delta\rho(\vec{r}') d\vec{r}'. \quad (2.39)$$

Here, $g(\vec{r}, \vec{r}')$ denotes the screened electron-electron operator, defined as

$$g(\vec{r}, \vec{r}') = \frac{1}{|\vec{r} - \vec{r}'|} + \frac{\delta^2 E_{exc}}{\delta\rho(\vec{r})\delta\rho(\vec{r}')} \Big|_{\rho_0}. \quad (2.40)$$

2.3 Effective form of the SP Hamiltonian in this work

When expressed in a proper basis of localized orbitals, the $E^{(1)}$ and $E^{(2)}$ terms acquire a form similar to common and well-known models in Solid State Physics: the tight-binding and the Hubbard model. Let us see them first.

2.3.1 Tight-binding model

The tight-binding model is a method commonly used to calculate the electronic band structure in solids using an approximate expression of the system's total wave function, written as superposition of wave functions corresponding to localized orbitals, being quite similar to the LCAO method. This approach turns out to be effective when describing highly localized electrons and it is complementary to the nearly free electron model. Even though the tight-binding model is a one-electron model, the idea may be extended to more sophisticated approaches and calculations.

We are now faced with solving the time-independent Schrödinger equation for a system made of a single electron under a periodic (crystalline) potential $V(\vec{r})$:

$$\hat{\mathcal{H}}|\phi(\vec{r})\rangle = \left[-\frac{\hbar}{2m}\nabla^2 + V(\vec{r}) \right] |\phi(\vec{r})\rangle = E|\phi(\vec{r})\rangle \quad ; \quad V(\vec{r} + \vec{R}) = V(\vec{r}), \quad (2.41)$$

where \vec{R} represents an arbitrary vector of the Bravais lattice. Since the crystalline potential is periodic, we already know that any solution of (2.41) must satisfy the **Bloch Theorem**:

$$|\phi_{n\vec{k}}(\vec{r})\rangle = e^{i\vec{k}\cdot\vec{r}} u_{n\vec{k}}(\vec{r}) \quad \text{with} \quad u_{n\vec{k}}(\vec{r} + \vec{R}) = u_{n\vec{k}}(\vec{r}). \quad (2.42)$$

Thus, our wave functions are characterized by two quantum numbers: a band index n and a wave vector \vec{k} . The main idea behind the tight binding model is to approximate our Bloch eigenstates $\phi_{n\vec{k}}(\vec{r})$ by a linear combination of highly localized atomic orbitals $\{\chi_{a\vec{R}}\}$, called *Wannier functions*. These are localized functions, equivalent to atomic orbitals and usually defined via Fourier transform of Bloch eigenstates:

$$|\chi_{a\vec{R}}\rangle = \frac{\Omega}{(2\pi)^3} \int_{1st \text{ BZ}} e^{-i\vec{k}\cdot\vec{R}} |\phi_{n\vec{k}}\rangle d\vec{k}. \quad (2.43)$$

Eq. (2.43) holds for a non-multiband case [20]. Ω denotes the volume of the primitive unit cell, and the integral is computed over all the first Brillouin zone (1st BZ). Wannier functions form a complete orthonormal set, and hence we may express any Bloch eigenstate in terms of them so that Bloch Theorem still holds:

$$|\phi_{n\vec{k}}\rangle = \sum_{\vec{R}} \sum_{a \text{ orbital}} e^{i\vec{k}\cdot(\vec{r}+\vec{R})} c_{n\vec{k},a} |\chi_{a\vec{R}}\rangle. \quad (2.44)$$

Now, we put the value of $|\phi_{n\vec{k}}\rangle$ into the Schrödinger equation in (2.41). Multiplying both sides by the bra $\langle\chi_{b\vec{R}'}|$, we may transform a set of eigenvalue equations into a set of algebraic equations:

$$\langle\chi_{b\vec{R}'}|\hat{\mathcal{H}}\sum_{\vec{R}}\sum_a e^{i\vec{k}\cdot(\vec{r}+\vec{R})}c_{n\vec{k},a}|\chi_{a\vec{R}}\rangle = \langle\chi_{b\vec{R}'}|\varepsilon_{n\vec{k}}\sum_{\vec{R}}\sum_a e^{i\vec{k}\cdot(\vec{r}+\vec{R})}c_{n\vec{k},a}|\chi_{a\vec{R}}\rangle. \quad (2.45)$$

Former expression may be rewritten as

$$\sum_{\vec{R}} \sum_a e^{i\vec{k}\cdot(\vec{r}+\vec{R})} c_{n\vec{k},a} \gamma_{b\vec{R}',a\vec{R}} = \varepsilon_{n,\vec{k}} \sum_{\vec{R}} \sum_a e^{i\vec{k}\cdot(\vec{r}+\vec{R})} c_{n\vec{k},a} \delta_{b\vec{R}',a\vec{R}}, \quad (2.46)$$

where

$$\gamma_{b\vec{R}',a\vec{R}} := \langle \chi_{b\vec{R}'} | \hat{\mathcal{H}} | \chi_{a\vec{R}} \rangle \quad \text{and} \quad \delta_{b\vec{R}',a\vec{R}} := \langle \chi_{b\vec{R}'} | \chi_{a\vec{R}} \rangle \quad (2.47)$$

are the *hopping* and the *overlap* integrals, respectively. Translational symmetry of our system allows us to write

$$\gamma_{b\vec{R}',a\vec{R}} = \gamma_{b\vec{R}',a\vec{R}-\vec{R}'} = \gamma_{b0,a\vec{R}} \equiv \gamma_{ba,\vec{R}} \quad (2.48)$$

and similarly for $\delta_{b\vec{R}',a\vec{R}}(\vec{k})$. Moreover, note that since we have chosen Wannier functions, which are orthogonal, the cross overlap terms vanish. Hence, we may rewrite (2.46) as follows:

$$\begin{aligned} \sum_a \underbrace{\left[\sum_{\vec{R}} e^{i\vec{k}\cdot(\vec{r}+\vec{R})} \gamma_{ba,\vec{R}} \right]}_{\Gamma_{a\vec{k}}} c_{n\vec{k},a} &= \varepsilon_{n\vec{k}} \sum_a \underbrace{\left[\sum_{\vec{R}} e^{i\vec{k}\cdot(\vec{r}+\vec{R})} \delta_{ba,\vec{R}} \right]}_{\Delta_{a\vec{k}}} \implies \\ &\implies \sum_a \left[\Gamma_{a\vec{k}} - \varepsilon_n(\vec{k}) \Delta_{a\vec{k}} \right] c_{n\vec{k},a} = 0. \end{aligned} \quad (2.49)$$

Note that the terms $\Gamma_{a\vec{k}}$ and $\Delta_{a\vec{k}}$ are, in fact, $N \times N$ matrices, whilst $c_{n\vec{k},a}$ represents a $N \times 1$ column vector. The procedure we consider is the following: For every \vec{k} in the Brillouin zone, or at least in a high symmetric region we are interested in, one must compute the hopping $\Gamma_{a\vec{k}}$ and overlap $\Delta_{a\vec{k}}$ matrices in \vec{k} -space. Then, Eq. (2.49) must be solved as a generalized eigenvalue problem and thus diagonalizing the hamiltonian. Eventually, we end up with N eigenvalues $\varepsilon_{n\vec{k}}$ for each \vec{k} , from which we may draw the sought electronic bands.

2.3.2 Two-electron interactions: Hubbard model

The former approach for the tight-binding (TB) model describes particles moving in a periodic potential using a hamiltonian written in terms of *Wannier orbitals* (see (2.44)), that is, highly localized wave functions $\{\chi_i\}$ centered on each atom. The *hopping* matrix element $\gamma_{ij} = \langle \chi_i | \hat{\mathcal{H}} | \chi_j \rangle$, defined for our purpose in (2.47), allows neighbour Wannier states to “hop”, or couple. In other words, they may interact with each other and hence hybridize. The eigenstates that we obtain by solving the set of equations depicted in eq. (2.49) are delocalized Bloch wave functions, as we are claiming that Bloch Theorem holds. One may see, for instance applying this model for a simple monoatomic H chain, that the band width gets broader as the hopping parameter γ increases.

The TB model cannot describe magnetic systems. In order to achieve this, it is necessary to explicitly include electron-electron interactions. One of the best examples is the Hubbard model (named after the British physicist John Hubbard who proposed it in 1963), which we have used constantly throughout this work.

In this model, the hamiltonian is made up of two different terms. The first one is exactly the same as in classical tight-binding model; a hopping term γ that describes the strength the electrons may hop with between lattice sites. The second term accounts for the Coulomb interaction between two electrons that occupy the same lattice site. In this situation, the energy is assumed to increase by an amount U . We may write the hamiltonian as follows [25]:

$$\hat{\mathcal{H}} = -\gamma \sum_{i,j=1}^N \sum_{\sigma} c_{i,\sigma}^{\dagger} c_{j,\sigma} + U \sum_{i=1}^N n_{i,\uparrow} n_{i,\downarrow}. \quad (2.50)$$

Here, $n_{i,\sigma} = c_{i,\sigma}^{\dagger} c_{i,\sigma}$ counts the number of electrons with spin σ at lattice site i . Therefore, this model includes the spin as quintessential element, making electrons with opposite spin on the same lattice site to repel each other via electrostatic interactions, and at the same time neglecting Coulomb interactions between electrons in different lattice sites. As in classical tight-binding model, the larger the hopping parameter γ is, the broader the band width will be, hence favouring a metallic phase. On the other side, the Hubbard term U penalizes occupation of a site with electrons that have the different spin. This means that if a lattice site already contains a certain density of electrons of a given spin, electrons with different spin will experiment a repulsion to hop there. In conclusion, the term U inhibits the hopping γ and both are constantly “competing” against each other.

Coming back to the overview of the SP-DFT (cf. [20] as we did), let us see how the TB model, and in addition the Hubbard model, look like when considering second-principles techniques. It is sensible first to express the electronic density in terms of Wannier functions:

$$\rho(\vec{r}) = \sum_{ab} d_{ab} \chi_{a\vec{r}} \chi_{b\vec{r}}, \quad (2.51)$$

where d_{ab} is the reduced density matrix. This matrix may be defined for the RED (i.e. $d_{ab}^{(0)}$, cf. [20]) to express $\rho_0(\vec{r})$. By means of this formalism, we can express the difference between the two densities defined in (2.34) by introducing a *deformation occupation matrix*:

$$\delta\rho(\vec{r}) = \sum_{ab} D_{ab} \chi_{a\vec{r}} \chi_{b\vec{r}}, \quad (2.52)$$

where $D_{ab} := d_{ab} - d_{ab}^{(0)}$. Using these definitions, we may to rewrite the first and second order terms for the SP-DFT energy as follows [20]

$$E^{(1)} = \sum_{ab} D_{ab} \gamma_{ab} \quad \text{and} \quad E^{(2)} = \frac{1}{2} \sum_{ab} \sum_{a'b'} D_{ab} D_{a'b'} U_{aba'b'}. \quad (2.53)$$

We have just introduced the parameters γ_{ab} and $U_{aba'b'}$ of our model whose role clearly resembles that of γ and U in the Hubbard model. They can be defined in terms of the Kohn-Sham hamiltonian \hat{h}_0 written in (2.38) and the Coulomb electron-electron interaction of (2.40):

$$\gamma_{ab} = \langle \chi_{a\vec{r}} | \hat{h}_0 | \chi_{b\vec{r}} \rangle \quad ; \quad U_{aba'b'} = \langle \chi_{a\vec{r}} \chi_{a'\vec{r}'} | \hat{g}(\vec{r}, \vec{r}') | \chi_{b\vec{r}} \chi_{b'\vec{r}'} \rangle. \quad (2.54)$$

However, for magnetic systems, we shall account for spin-polarized density, and so the previous definitions must be adapted. In this way, we may write $E^{(2)}$ in terms of Hubbard (U) and Stoner (I , cf. [25])-like parameters as follows (see [20] for more details about the terms involved):

$$E^{(2)} = \frac{1}{2} \sum_{ab} \sum_{a'b'} \left[(D_{ab}^{\uparrow} + D_{ab}^{\downarrow})(D_{a'b'}^{\uparrow} + D_{a'b'}^{\downarrow}) U_{aba'b'} - (D_{ab}^{\uparrow} - D_{ab}^{\downarrow})(D_{a'b'}^{\uparrow} - D_{a'b'}^{\downarrow}) I_{aba'b'} \right]. \quad (2.55)$$

Recall that the aforementioned parameters are **not** those appearing in the Hubbard model. To simulate it, we must impose $U_{aba'b'} = I_{aba'b'}$. Furthermore, as in the Hubbard model we only account for on-site interactions, the former parameters must be diagonal.

2.4 Monte Carlo method and implementation in this work

In Solid State Physics, we usually handle systems made of a large number of particles. Therefore, it is not computationally feasible to treat the motion of all of them by means of a rigorous quantum-mechanical-based model. However, in many cases, we are more interested in macroscopic properties (i.e., how the system “behaves” as a whole) rather than in microscopic information. An immediate example comes for the purpose of this work; if we are pursuing a magnetic transition in a certain system, we are only interested in how the global spin correlation adds up, no matter how the *exact* spin of every single particle looks like. In other words, we are not tracking the microstate in which the system is located at every time, but the macrostate. The existence of a huge number of coupled degrees of freedom, due to the large number of particles involved in our problem, leaves no room for a deterministic approach. In this situation, the Monte Carlo methods offer a powerful way to numerically solve the problem of fluctuation or relaxation in stochastic systems [21].

In principle, Monte Carlo methods may be used to solve problems that have a probabilistic interpretation by performing a random sampling through as many significant microstates as possible. Then, if the number of visited microstates is sufficiently large, an average will yield a representative “picture” of our system at a certain time. Let us take a succinct look on the statistical foundations of the Monte Carlo methods within this work’s scope of study, following the reference [21]. We are interested in how the global spin correlation function (i.e. magnetization) \mathcal{C} evolves with the time t , so basically our problem may be described, for a certain temperature, by a set of random variables $\{X_n\} \equiv \{\mathcal{C}_n\}$. Recall that a random variable

$$X : (\Omega, \sigma, \mathbb{P}) \rightarrow \mathbb{R}$$

is a measurable map defined on a probability space $(\Omega, \sigma, \mathbb{P})$. Here, Ω denotes our sample space containing all the possible outcomes of an experiment, $\sigma \subseteq \mathcal{P}(\Omega)$ the σ -algebra of all the possible events and $\mathbb{P} : \sigma \rightarrow [0, 1]$ the probability function. The random variable X determines a unique distribution function, $F : \mathbb{R} \rightarrow [0, 1]$ defined as:

$$F_X(t) := \mathbb{P}(X \leq t) \equiv \mathbb{P}(\{\omega \in \Omega : X(\omega) \leq t\}) \text{ for } t \in \mathbb{R}. \quad (2.56)$$

The forthcoming discussion requires the following two assumptions:

- i) Our random variables X_n are equally distributed, i.e., the distribution functions F_{X_n} are all the same. Moreover, it should hold for the expected value $\mathbb{E}(|X_1|) = \dots = \mathbb{E}(|X_n|) = \dots < \infty$.
- ii) Our random variables are stochastically independent. That is, for every indexes n, m the joint cumulative distribution function satisfies

$$F_{X_n, X_m}(s, t) = F_{X_n}(s) \cdot F_{X_m}(t). \quad (2.57)$$

Intuitively, *ii*) means that the result of one variable does not affect the probability of occurrence of the others. Now, we are in conditions to enunciate the following theorem:

Theorem 2.4. (Strong Law of Large Numbers) *Let X_1, X_2, X_3, \dots be a sequence of independent, equally distributed random variables with $\mathbb{E}(|X_1|) < \infty$ and expected value μ . Let*

$$\bar{X}_n = \frac{X_1 + \dots + X_n}{n} \quad (2.58)$$

be the sample mean. Then it holds

$$\bar{X}_n \xrightarrow{a.s.} \mu \iff \mathbb{P}(\{\omega \in \Omega : \lim_{n \rightarrow \infty} \bar{X}_n(\omega) = \mu\}) = 1. \quad (2.59)$$

That is, the sequence converges almost sure (i.e. with probability 1, except for a set of measure zero) to μ .

The Strong Law of Large Numbers is crucial for our analysis, and its interpretation is clear: the more events we measure (assuming those events are distributed in the same way and that there is no bias coming from previous measurements), the closer will be the sample average with respect to the value we would like to estimate.

Now, using Theorem (2.4), it would be straightforward to implement a Monte Carlo method, provided a certain probability distribution to generate the sample X_1, \dots, X_n , for instance a classical Maxwell-Boltzmann (MB) distribution. However, can we assume that these random variables are equally distributed in that way? The answer is in general negative, and that is the reason why Monte Carlo techniques may sometimes face non-tractable situations. Thus, we must find a way to sample microstates so that the probability distribution does not vary as we keep on simulating.

The Metropolis-Hastings algorithm, named after Metropolis [23] and Hastings [24], proposes a way to construct a stochastic process that reaches a certain stationary distribution. This algorithm is based on constructing a Markov chain, which may be defined as a stochastic process X_1, \dots, X_n verifying the following for the conditional probability:

$$\mathbb{P}(X_{n+1} = x_{n+1} \mid X_n = x_n, \dots, X_2 = x_2, X_1 = x_1) = \mathbb{P}(X_{n+1} = x_{n+1} \mid X_n = x_n). \quad (2.60)$$

That is, the probability of moving to the next state depends only on the current state, regardless of the previous ones. In other words, our system has no “long-term memory”. Without going into too much detail (further description may be found in the papers of Metropolis [23] and Hastings [24], as well as in [21]), we may construct a Markov chain satisfying:

- i) **Stationariness.** There exists a distribution π and a natural number $k \in \mathbb{N}$ such that $X_n \sim \pi$ for each $n \geq k$. Thus, from a certain index onwards, the distributions of the random variables are (almost sure) identical.
- ii) **Ergodicity.** Roughly speaking, this condition means that we can reach any state starting from any other state with a non-zero probability. This property implies that we may substitute the ensemble average of a certain physical property by the corresponding time average.

Translated into physical terms, reaching a stationary probability distribution is equivalent to reaching a thermal-equilibrium state. Hence, according to Statistical Mechanics, a system at thermal equilibrium may be described by means of the canonical ensemble (also called NVT ensemble since number of particles, volume and temperature are fixed thermodynamical variables) and the corresponding Maxwell-Boltzmann statistics:

$$\mathbb{P}(X = x) \equiv p^{eq}(x) = \frac{e^{-\frac{E(x)}{k_B T}}}{\mathcal{Z}}, \quad (2.61)$$

where $E(x)$ denotes the whole energy of the system having a dynamical variable x (in our case the spin distribution), k_B is the Boltzmann constant and T is the temperature. The denominator, named after the German word *Zustandssumme*, is the partition function of our system:

$$\mathcal{Z} = \sum_{i=1}^N e^{\frac{-E(x_i)}{k_B T}}. \quad (2.62)$$

The system needs a certain time to thermalize ,i.e., to reach the thermal-equilibrium state relative to the given temperature. Therefore, the total number of sweeps N_s is divided into thermalization sweeps N_t and run sweeps N_r so that $N_s = N_t + N_r$. We shall just store the correlation after the thermalization has taken place and in steps that are sufficiently far from each other, thus making one event being independent from the all the previous ones as we claim in Eq. (2.60) for a Markov chain. The version of the Metropolis-Hastings algorithm considered in this work adopts this quite simple form:

INPUT: $L \times L$ initial configuration, array T with temperatures and number of sweeps N_s , thermalization steps N_t
 C = empty array to fill with correlations
 S = empty array to fill with standard deviations
for t in T **do:**
 C_{inst} = empty array to fill with instant correlations
for $n=1$ **to** N_s **do:**
for $i=1$ **to** L^2 **do:**
Calculate energy difference ΔE of the new state relative to the former one
if $\Delta E \leq 0$ **then:**
Update to the new state
else:
Generate a random number $r \in (0, 1)$
if: $\exp(-\Delta E/k_B T) > r$ **then:**
Update to the new state
else:
Leave the state as it is
end if
end if
end for
if: $n > N_t$ **do:**
Add current correlation to C_{inst}
end if
end for
Add to C mean value of C_{inst}
Add to S standard deviation of C_{inst}
end for
RETURN: C and S

Chapter 3

Results

Once we have thoroughly explained the computational methods, we may now start to present the main results obtained in this work. We shall begin by introducing the model for the CuO_2 layers found in La_2CuO_4 , describing their electronic structure through a set of Wannier functions. We shall commence our analysis by presenting a simple TB model on our CuO_2 layers. Then, we will proof how SP-DFT techniques reproduce both the FM and the AFM states, depicting their corresponding energies, density of states (DOS) and band structure. We will also show how the electronic hamiltonian for this system is written in terms of the γ and U parameters introduced in Chapter 2 and how the phase transition depends on their ratio.

The next step consists in evaluating the correlation as a function of the energy. As we will see, the FM (resp. AFM) microstate presents both highest (resp. lowest) energy and correlation. A simple glance on these results will suffice to figure out whether there is a population of microstates valid for our Monte Carlo method.

We will finish this chapter by presenting the simultaneous AFM-paramagnetic and insulator-metal phase transition achieved thanks to the Monte Carlo simulation, arguing changes of spin correlation and DOS.

Contents

3.1 Model employed	29
3.2 FM vs AFM	30
3.3 Importance of U/γ	32
3.4 Correlation as function of energy. Microstates	34
3.5 AFM insulator- paramagnetic metal phase transition during MC	37

3.1 Model employed

As we mentioned in the first chapter, the relevant orbitals on the CuO_2 are $Cu^{2+} d_{x^2-y^2}$ and $O^{2-} p_x, p_y$. The conduction band may be properly described as arising from a single, hybridized orbital. If we take a look at the energy scheme (see figure 3.1), we may see that this hybrid orbital turns out to have a much larger Cu-like contribution, while the lower energy fully occupied band displays a predominately O-like character

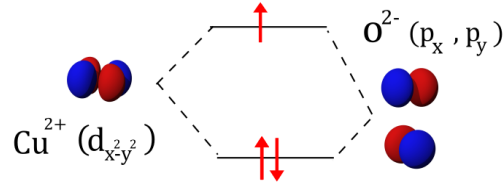


Figure 3.1: *Bonding scheme for the interaction between $\text{Cu}^{2+} d_{x^2-y^2}$ and $\text{O}^{2-} p_x, p_y$ WF orbitals .*

Without going into further details, we may state the main ansatz of our approach: the two-dimensional CuO_2 system may be described by a supercell where on each lattice site there is only one single WF orbital. Moreover, the fact that the WF orbitals are localized on each lattice site allows us to simplify our problem by just considering a Hubbard-like system whose character is $\text{Cu}(3d_{x^2-y^2})$.

3.2 FM vs AFM

Now that we have established the basis of our model, let us proceed with the first results. First of all, we may start by observing how SCALE-UP is able to reproduce the TB model on a two dimensional lattice:

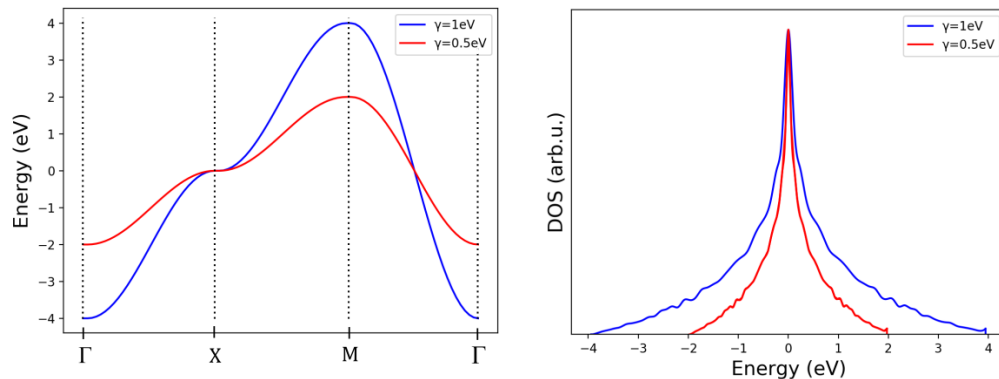


Figure 3.2: *Tight binding model bands (left) and density of states (right) for values of the hopping parameter $\gamma = 1 \text{ eV}$ (blue) and $\gamma = 0.5 \text{ eV}$ (red). The supercell taken has size 2×2 . We may notice that the band width depends strongly on the value of γ . The energy axis has been set to have its origin at the Fermi energy.*

As a result of interaction between Wannier orbitals, the corresponding level has broadened forming a band with a width $W = 8\gamma$.

It turns out clearly that the bigger the hopping parameter γ , the wider the band. This fact resembles the meaning of γ exactly as we defined it: the more overlap between orbitals, the larger the hopping will be, and thus the electrons may tunnel between the wells of the crystalline potential much easier. Therefore, wider bands usually (it really depends on occupation as well) correspond to metallic systems, where there is no energy gap.

Moving on, we are going to handle magnetic systems by means of a SP-DFT Hubbard-like model. The first thing we must accomplish is to figure out that the AFM configuration is indeed the least energetic, whilst the FM system has the largest energy. For the sake of simplicity, we may deal with

a simple 2×2 lattice in order to explore all the possible configurations. It is straightforward to see that there are just four different configurations.

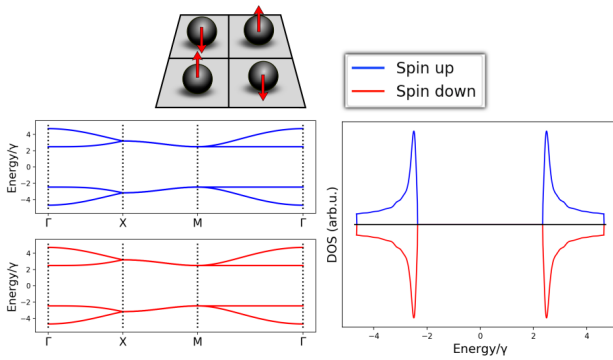


Figure 3.3: *Antiferromagnetic (AFM) configuration, total energy $E = -8.374305 \gamma$.*

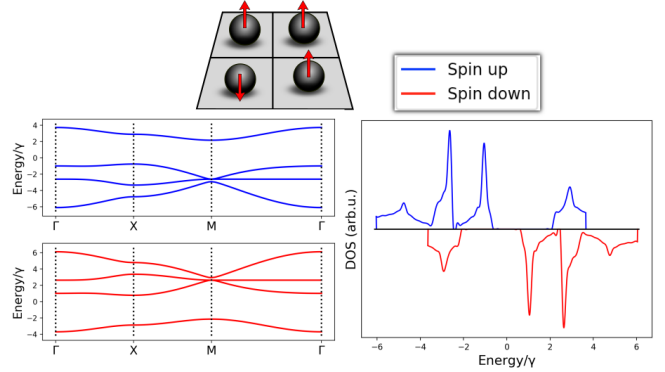


Figure 3.4: *Intermediate configuration, total energy $E = -7.402935 \gamma$.*

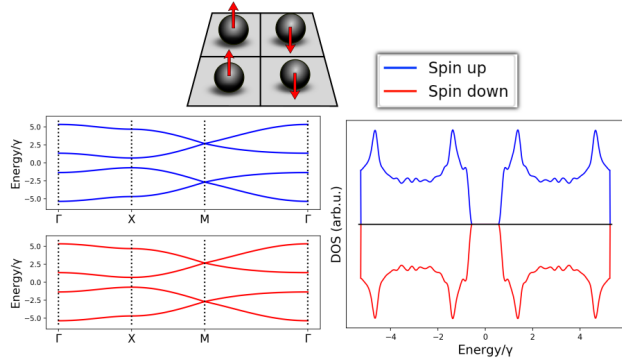


Figure 3.5: *Intermediate configuration, total energy $E = -7.29945 \gamma$.*

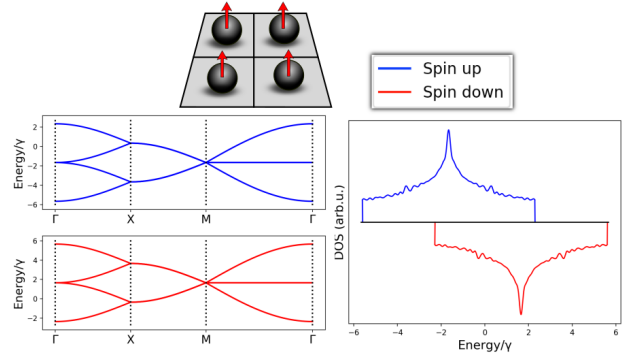


Figure 3.6: *Ferromagnetic (FM) configuration, total energy $E = -6.760775 \gamma$.*

In the figures above we have just depicted the bands structure and the DOS for all the different spin configurations, setting $\gamma = 2 \text{ eV}$ and $U = 3\gamma = 6 \text{ eV}$. Other dispositions are equivalent, as we would end up with an equal system up to a translation. Regarding the units, we simply represent the energy in terms of the hopping parameter γ , i.e., as a multiple of it.

Indeed, we have just verified that the AFM configuration is our ground state, whereas the FM one corresponds to an energy maximum, and is thus unstable. Other possible configurations have an intermediate energy and build up an energy/spin correlation spectrum that we will present afterwards.

There is also a noticeable fact connected to the former plots. Although there exist only four different microstates, which do not let any room for a rigorous statistical and physical analysis, we may note that the ground state (AFM) starts being an insulator as mentioned in the first chapter. For the sake of clarity, it is recommendable to take a look at the DOS plot to observe the large gap that characterizes our current state.

As a matter of fact, it is clear that the insulating behaviour vanishes as we increase the spin correlation (i.e., we move towards a more paramagnetic configuration). Still the intermediate configurations do have an energy gap, though significantly smaller. Finally, the FM configuration is purely metallic. Bearing in mind that a 2×2 lattice is not large enough to rigorously reproduce a

phase transition, this simple example suffices to demonstrate that the objective we are pursuing is feasible within our framework.

3.3 Importance of U/γ

It should be noted that for a Hubbard-like model the quantity U/γ plays a crucial role. In our La_2CuO_4 we are neglecting lattice (and thus phonon) effects and hence the total energy is approximated by the sum of first order $E^{(1)}$ and second order terms $E^{(2)}$ (neglecting the zeroth term that describes the lattice itself), we may express the aforementioned energy in terms of U/γ by simply dividing by γ :

$$\frac{E_{DFT}}{\gamma} \approx \sum_{ab} D_{ab} + \frac{U}{\gamma} \sum_{ab} \sum_{a'b'} D_{ab} D_{a'b'}. \quad (3.1)$$

Within this approach, the hopping parameter simply scales the Hamiltonian.

The first fact we shall find out is to what extent the factor U/γ affects not also the shape of microstates population sorted by energy, but also the system's character itself. A way to figure it out is to observe how distant the FM and the AFM configurations are from each other as we vary both U and γ .

Naively, our ansatz for this problem would be that the smaller U/γ , the larger metallic character of our system: large γ means that electrons present a tendency to jump to neighbouring lattice sites, thus increasing system's conductivity. At the same time, a small value of U means small inhibition between electrons occupying the same orbitals which, again, contributes to mobility. Insulating character should occur in an opposite situation, precisely when $U/\gamma \gg$. This behaviour may be easily observed by means of a simple calculation on a 2×2 lattice (see Fig. 3.7).

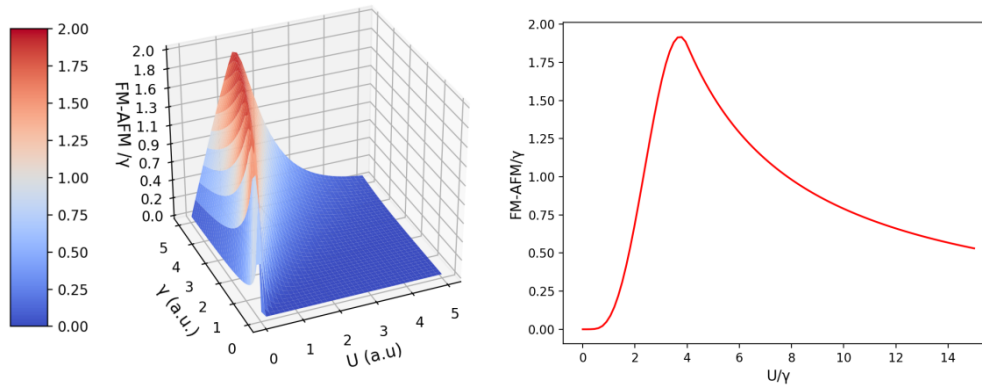


Figure 3.7: **Left:** 3d plot energy difference between FM and AFM as a function of both U and γ . **Right:** 2d plot of the same value as a function of U/γ . The simulations have been performed on a 2×2 lattice and choosing a sample of 30×30 k -points within the first Brillouin zone.

The purpose of the 3d plot in Fig. 3.7 is to find out whether U and γ themselves influence the value of the energy difference. It turns out that, regardless of the value of both parameters, the shape of the function only depends on the quotient U/γ . Essentially, we may observe that our function reaches a maximum at about $U/\gamma \sim 3.7$ and goes to zero both at $U/\gamma \approx 0$ as well as at large U/γ values. In our model, there is a continuous concurrence between covalence (represented by the hopping parameter γ and favouring delocalization) and repulsion (arising from the Hubbard

parameter U and causing localization). This maximum represents the point where the localization is the highest possible. Needless to say, both contributions are needed in order to understand magnetism. Another remarkable fact is that FM and AFM configurations coincide in both limits $U/\gamma = 0$ and $U/\gamma \rightarrow \infty$:

- i) $U \ll \gamma$: In this case we may argue as if U were zero. Under such circumstances, our hamiltonian resembles the one of a tight-binding-like model. Since we do not take spin (or magnetism) into account, AFM and FM states are equal and coincide with the metallic solution without spin polarization.
- ii) $U \gg \gamma$: This case is reasonably described by a model with $\gamma = 0$. In this situation there is no hopping, the electrons are completely localized (or isolated) at each lattice site. As if we had cut off the covalent bonds between neighbouring orbitals, both AFM and FM states present the same energy for this reason.

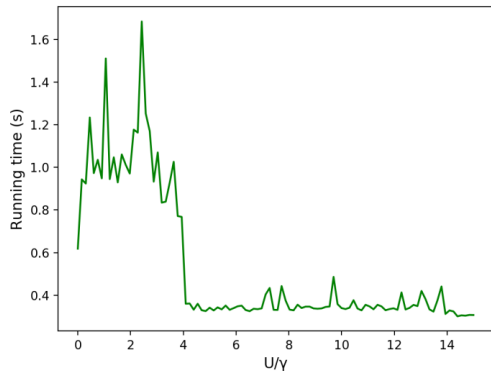


Figure 3.8: *Running time (half the sum of running time for FM and that of AFM) for simulations depicted in 3.7 (right).*

If we take a look at the computation times on Figure 3.8, we may note that it takes much more for SCALE-UP to converge below the maximum of the afore-presented curve, at $U \sim 4\gamma$. These time-demanding cases are precisely the ones with a high covalent character and mobility, where interatomic interactions, rather than intraatomic ones, play a crucial role. Moreover, it turns out that these values for U/γ require a larger k-sampling in order to assure convergence. The states with higher correlation (which perform as metals) are by far the most time-demanding ones. This may be a severe issue when trying to randomly explore microstates during

the MC, as having no convergence for certain configurations might bring a bias into our calculation.

The results in Figure 3.8 point out that at some point below $U \sim 4\gamma$ the system's behaviour changes. As we have depicted half the sum of the computation times for AFM and FM configurations, let us take a look at these for various values of U/γ .

As we can see in the plots in Fig. 3.9, the AFM configuration is clearly an insulator for almost every value of U/γ , though at $U/\gamma \sim 0.5$ and below this state resembles the metallic TB solution, being quite similar to the FM solution as already explained. Unlike in a one dimensional case, this metal-insulator transition of the AFM solution takes place gradually. However, the most relevant fact we can conclude from Figure 3.9 is that the FM configuration is no longer a metal above $U/\gamma \sim 4$. As we may note, spin up and spin down channels distance themselves from each other and the system becomes an insulator. The reason for a low convergence relies on the “entanglement” among bands of both channels below this threshold. Consequently, as it turns out that not only FM but also many other intermediate states present this character, there is no reason to seek an insulator-metal transition above this limit. There would not be **any** metallic state, not even the FM. Nevertheless, a magnetic transition would take place regardless the value of U/γ .

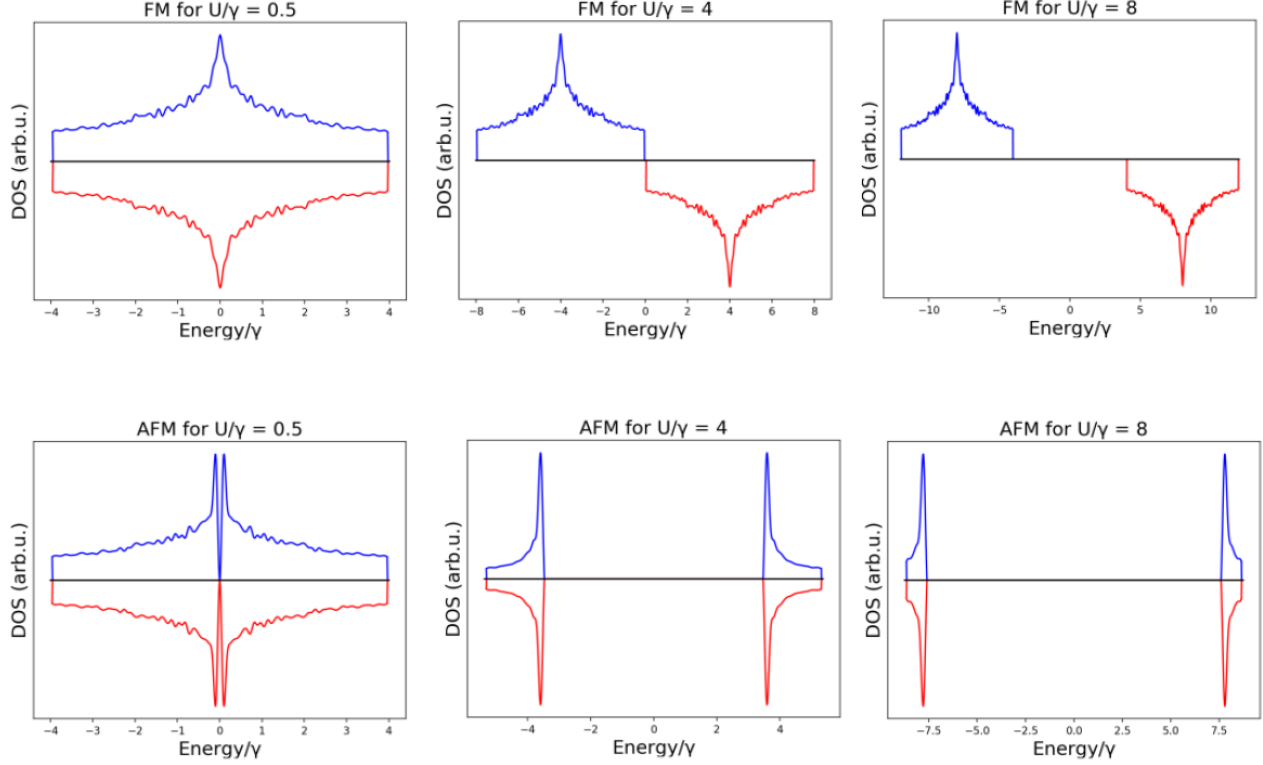


Figure 3.9: *FM state (up) and AFM state (down) por $U/\gamma = 0.5, 4$ and 8 .*

3.4 Correlation as function of energy. Microstates

In order to account for magnetic ordering in a large supercell where magnetic disordered states can be simulated, we shall proceed quantitatively. That is, we must introduce a quantity that helps us to identify magnetic structures. Given a $N \times N$ supercell with one atom per lattice site, the easiest way to approach this problem it is by defining *x- and y- spin correlation functions*:

$$C_x = \frac{1}{N^2} \sum_{\substack{i,j=1 \\ i \neq j}}^N S(i, j) \cdot S(i+1, j) \quad \text{resp.} \quad C_y = \frac{1}{N^2} \sum_{\substack{i,j=1 \\ i \neq j}}^N S(i, j) \cdot S(i, j+1), \quad (3.2)$$

where $S(i, j)$ represents the spin at the position (i, j) and the former expressions are normalized so that they can be 1 at most (or -1 at least). Furthermore, we shall choose adequate periodic boundary conditions (PBCs) by “folding around” our system as if it were a torus. Quantitatively, this means that we impose that both indexes i and j are integers module N . In particular,

$$S(N+1, j) = S(1, j) \text{ and } S(i, N+1) = S(i, 1) \text{ for every } i, j.$$

The *total spin correlation* is defined as half the sum of the formers, i.e., $\mathcal{C} = \frac{1}{2}(C_x + C_y)$. Taking this function as mean to characterize the ferromagnetic (or antiferromagnetic) behaviour of any system, it is straightforward to see that a pure FM (resp. AFM) configuration has a maximum (resp. minimum) value for \mathcal{C} . If all the spins were either $+1$ or -1 , those values would be $+1$ resp. -1 as well. Although we provide such $+1/-1$ configuration as input for the SCALE-UP code, we might not end up with a similar lattice, but rather a system whose electrons are not localized at each lattice site

and thus handling a spin density distribution. As we will see, that is a meaningless quantitative issue, since FM and AFM are still the configurations with highest and lowest correlation and we may express the rest in terms of them by simply normalizing.

We have already observed how the factor U/γ determines how far away the FM and AFM configurations are from each other, including the time cost of our simulations and where we expect an insulator-metal transition phase to occur. Now, we shall go deeper by taking the correlation into account. As a matter of fact, we expect the correlation to rise as the energy does, being FM and AFM the extreme cases. At the same time, we are also interested in sketching out the microstates' energy population. Since we set all the spins to be $+1$ or -1 on the input lattice, the population for the input configuration presents a discrete distribution. It is essential to highlight that, although it might seem true at first glance, that distribution is not binomial. The reason is that we do not have a sum of independent Bernoulli distribution (neighbour spins aligned or not with same probability), but they are in fact dependent due to the PBCs and the fact that x-correlation and y-correlation are stochastically dependent. However, and since electrons delocalize, we must deal with a spin density (i.e. arbitrary numbers in $(-1, 1)$) rather than with $+1$ or -1 . Thus, it is definitely not true that the magnetic order may be properly described by means of a discrete probability distribution. We now aim to figure out whether the normal distribution is an adequate option.

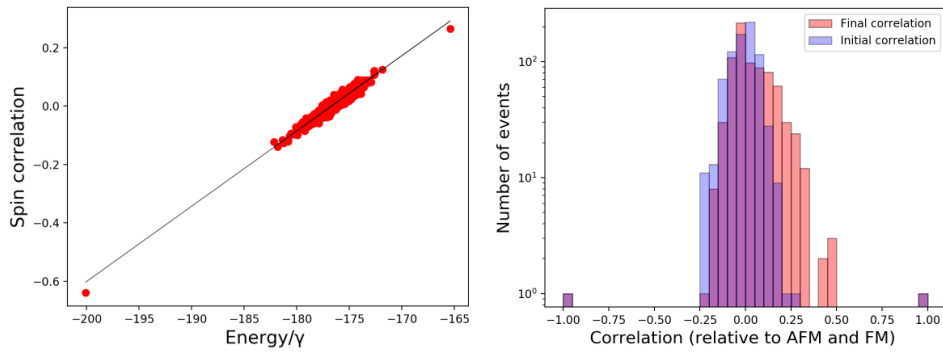


Figure 3.10: **Left:** Non-normalized spin correlation vs energy in γ units and linear fit, which yields $R = 0.97612689$. **Right:** Normalized correlation histogram. These data correspond to $U/\gamma = 2.72$.

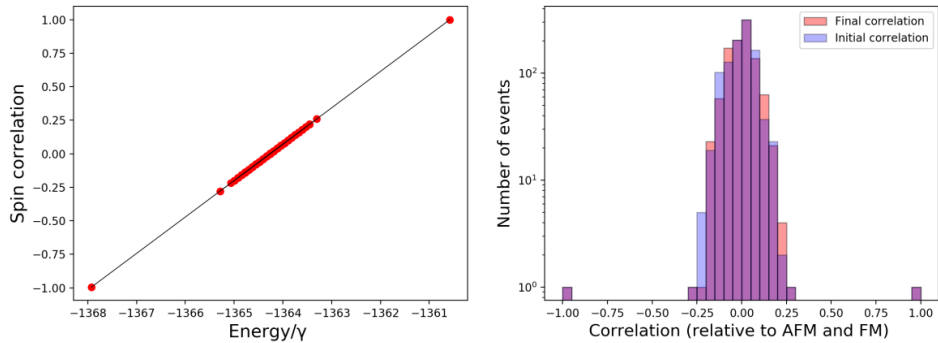


Figure 3.11: **Left:** Non-normalized spin correlation vs energy in γ units and linear fit, which yields $R = 0.99999929$. **Right:** Normalized correlation histogram. These data correspond to $U/\gamma = 27.2$.

These data have been achieved by running 1000 SCALE-UP simulations using a fixed $\gamma = 2eV$ and

$U = 0.2$ and 2 u.a. For each simulation, a completely random lattice was generated. Note that the FM and AFM initial configurations have been intentionally introduced.

In the former plots we have just shown, on the one hand, a linear fit of the correlation (not normalized in terms of AFM and FM correlations) against the energy. We may verify what we were intending to show, namely that the correlation is directly proportional to the system’s energy. These plots point out in the same direction as the Figures 3.3, 3.4, 3.5 and 3.6 did, but for much larger dimensions, that the AFM configuration turns out to be an energy minimum, whereas the FM state is a maximum. Large correlation coefficients, shown on the caption, give a quantitative idea of how good spin correlation and energy correlate. It is also worth mentioning that the smaller the U/γ factor, the more spread the points are. As we mentioned earlier, $U/\gamma < 4$ implies spin up and down bands close to each other in energy, and there is higher covalence and delocalization. Conversely, if we increase the quotient above this threshold, there is no metallic state the code must handle. Hence, huge localization at each lattice site and weak interactions among neighbouring Wannier orbitals lead to an almost perfect correlation where every point lies roughly on the fit line.

This reasoning holds for the correlation histograms too. As expected, systems with localized electrons present little changes on spin density before and after running a simulation. Let us try to account how these changes may be quantified. First, we insist that the initial correlation may not be described by a binomial function. In fact, coming up with the right distribution function is not a trivial issue. Instead, we can focus on the final correlation distribution, which is actually the one that matters. The most immediate question it may arise is whether taking a normal distribution is sensible. For a first glance, let us consider the following Q-Q plots in the Figure 3.12 below.

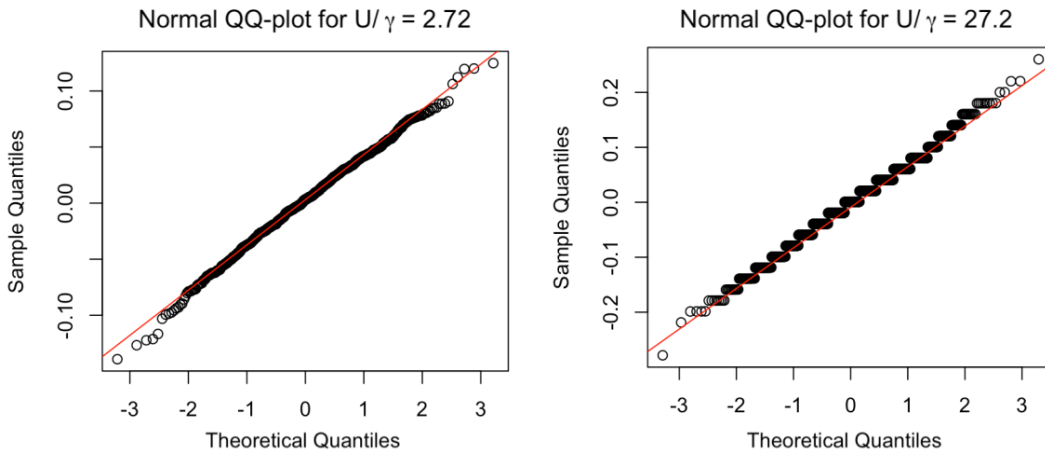


Figure 3.12: *Q-Q plots for $U/\gamma = 2.72$ and $U/\gamma = 27.2$ (values of Figures 3.10 and 3.11). Sample quantiles are plotted against those of a $\mathcal{N}(0, 1)$. A red straight line passing through the 0.25 and 0.75 quantiles has been drawn.*

Q-Q plots intend to plot the sample quantiles against those of a normal distribution $\mathcal{N}(0, 1)$. They are used in order to estimate whether the sample distribution looks normal, although other distributions may be considered as well. In our case, the spin correlation distribution for $U/\gamma = 2.72$ turns out to be normal in appearance, though we must insist that Q-Q plots are not sufficient to prove normality, but rather to dismiss it. On the other hand, as the sample for $U/\gamma = 27.2$ presents little changes on the correlation with respect to the initial one, it does not appear to be normally distributed at all. This remaining “discreteness” of our sample may be observed on the Q-Q plot: the quantile function, or equivalently, the inverse of the cumulative function distribution, is not

continuous. Going even further, we may also seek for evidence of normality of our sample $\mathcal{C}_1, \dots, \mathcal{C}_n$ by means of the Shapiro–Wilk test (cf. the original paper from Shapiro and Wilk [27]). Null- and alternative hypotheses for this test are:

$$H_0 : \mathcal{C}_1, \dots, \mathcal{C}_n \text{ are normally distributed.}$$

$$H_a : \mathcal{C}_1, \dots, \mathcal{C}_n \text{ are **not** normally distributed.}$$

The function `shapiro.test()` of RStudio (see RDocumentation) yields a p-value of 0.2134 and $5.934 \cdot 10^{-5}$ for the cases $U/\gamma = 2.72$ and $U/\gamma = 27.2$, respectively. As anticipated, it is very unlikely that the null hypothesis holds when $U/\gamma = 27.2$, so we can confidently reject it. For $U/\gamma = 2.72$, there is a high 21.34 % chance of failure if H_0 is rejected, so we shall not. Recall that keeping the null hypothesis H_0 does not mean that it holds, but that there is not enough statistical evidence to assert that H_a does. In other words, a test hypothesis is only valid to prove the falseness of an assertion, but **not its veracity**.

Summing up, there is *a priori* no way to sketch the correlation distribution function. And, if we could, it is not fully clear whether we might take advantage of it for the purpose of this research. For instance, randomly sampling from a given normal distribution would not give us actual microstates of our system, but a continuum of energies (or correlation). This approach would hence hinder our aim to resemble temperature fluctuations and assessing accessible microstates in terms of the thermal excitation. For this reason, we may ignore how the actual correlation distribution might look like and focus instead on a Monte Carlo approach that will allow us to reproduce the effect of the temperature on our system.

3.5 AFM insulator - paramagnetic metal phase transition during MC

So far in the previous sections, a systematic characterization of our system has been our goal. First, we aimed to prove, by means of calculations on a 2×2 lattice, that the energy minimum (resp. maximum) corresponds to the antiferromagnetic (resp. ferromagnetic configuration). This point is crucial in case we would like to achieve an insulator-metal transition. As second step, we have figured out the influence of the parameter U/γ on our system's behaviour, arguing its relevance in order to fully understand the magnetism, and how the electronic properties of both AFM and FM vary while U/γ does. In particular, we have established a threshold at about $U/\gamma \sim 4$ below which we should expect an insulator-metal phase transition to take place.

The third element to take into account is the spin correlation, which allows us to classify the magnetic ordering of any microstate. Moreover, we have successfully evidenced the excellent correlation between this variable and the system's energy, concluding that the higher the correlation, the higher the energy. The sharp, nearly zero-centred correlation histograms in Figures 3.10 and 3.11 pave the way for a MC simulation, since the correlation distribution seems to be concentrated at paramagnetic states, whilst those close to the AFM and FM configurations appear to be more seldom.

All these aforementioned elements are crucial in order to understand why and how we carry out a MC procedure. As mentioned in the previous chapter, we have utilized a simple version of the Metropolis-Hastings algorithm, taking Maxwell-Boltzmann (see Eq. (2.61)) as stationary distribution. For the sake of significance, we have intended to perform a MC on a 10×10 lattice, choosing $U = 5.44$ eV (i.e. 0.2 u.a.) and $\gamma = 2$ eV as parameters. Therefore, $U/\gamma = 2.72$ remains within the range where

we expect a phase transition to happen. Nevertheless, these simulations require a huge amount of time to be successfully carried out. Having no access to the computational tools from mid-March onwards has led to a somehow limited MC. However, it does suffice for what we are pursuing, namely for observing an insulator-metal phase transition:

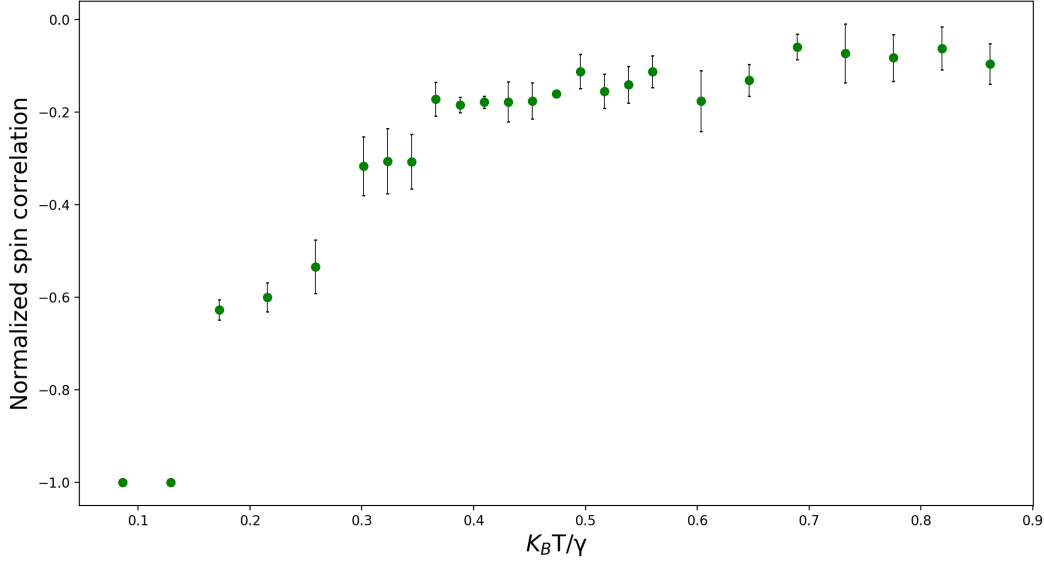


Figure 3.13: Normalized correlation as a function of the thermal excitation, scaled by the hopping parameter γ . Normalization is carried out by dividing positive values by the FM correlation, whereas negative ones are divided by that of the AFM state. The values plotted are the average of those sampled during the Monte Carlo after the thermalization and sufficiently far away from each other in order to accomplish the Markov chain condition (see M-H algorithm). The error bars correspond to the statistical standard deviation. 15 sweeps have been performed, from which 6 are thermalization steps.

Figure 3.13 depicts the spin correlation (normalized in terms of FM and AFM states) as a function of the temperature. All thermal excitations are expressed in γ factors.

For the sake of simplicity, we have just started from an antiferromagnetic configuration, i.e., the ground state. As expected, at low temperatures the correlation remains at a minimum, pointing out that the AFM is the only accessible state. When the temperature increases, more states become accessible and eventually get sampled along our MC. While the average energy increases, so does the average correlation at each temperature, and thus the initial AFM ordering disappears gradually until, for a sufficiently large temperature, all microstates (or an overwhelming majority of them) are accessible. This means that all configurations are equally probable, and therefore the mean correlation tends to adopt a steady value close to zero which corresponds to that of the correlation distribution (cf. Figure 3.10) and a paramagnetic behaviour.

This behaviour represents a magnetic phase transition, and we could have assumed it to be true even before running a MC, just by briefly observing how the correlation distribution looks like in Figures 3.10 and 3.11. However, in order to assess the insulator-metal phase transition, which shall occur simultaneously, we must take a look at the electronic properties (reflected on the band structure and the DOS), and their evolution along the simulation. Let us take a deeper look at the DOS and the spin density for various states:

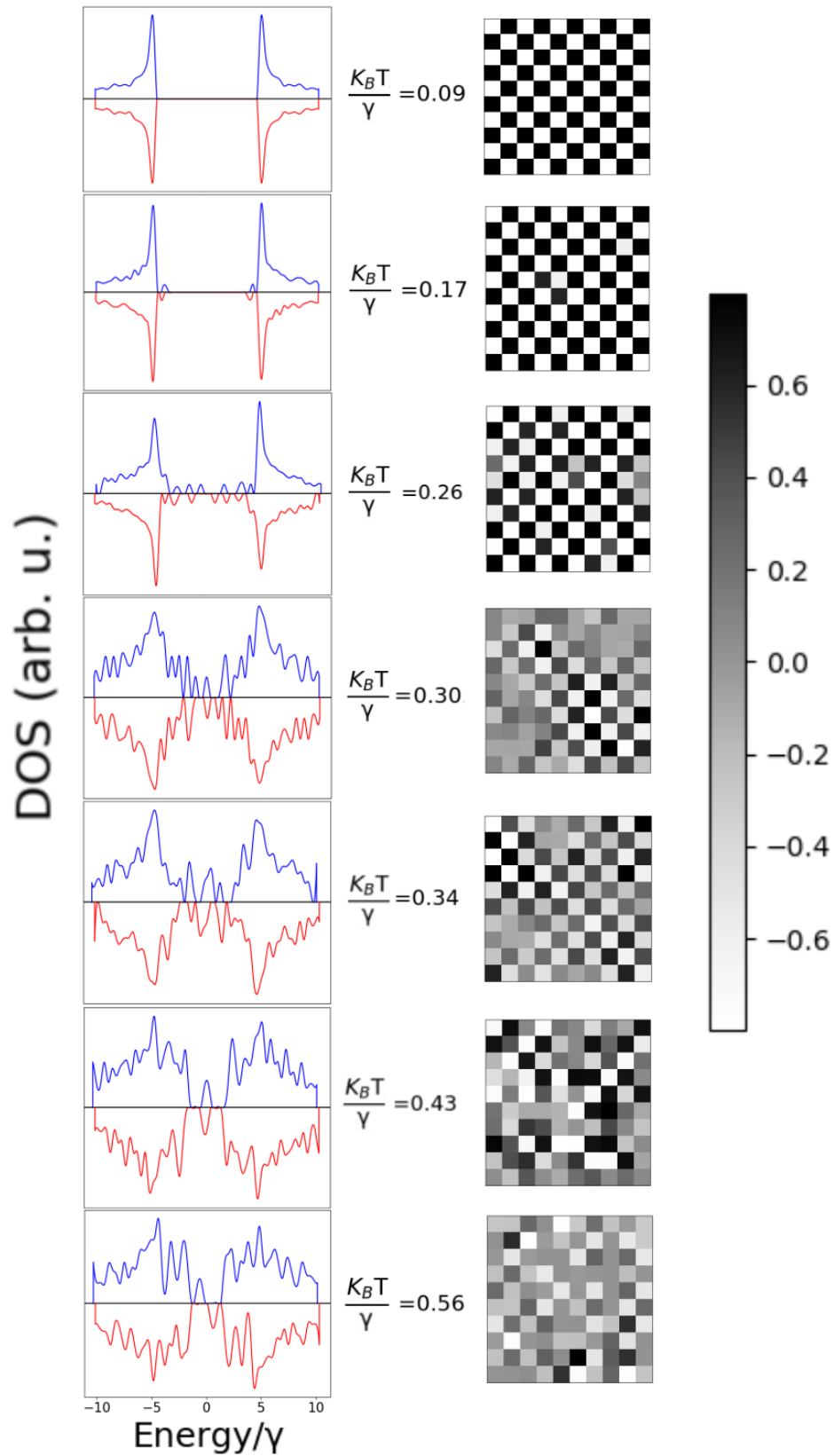


Figure 3.14: Density of states (left) from seven points taken from 3.13 is depicted. For each DOS, the corresponding spin distribution (right) is depicted with a grayscale.

Figure 3.14 yields an illustrative depiction of both processes: The AFM-paramagnetic phase transition is reflected on the lattice grayscale representation, which indicates the magnetic ordering and is complementary to Fig 3.13. The insulator-metal transition may be observed in the evolution of the DOS.

As we can see, at low temperatures the system's preferred configuration is that of an antiferromagnetic insulator, as no thermal excitations arise. Slightly increasing the temperature leads to a tiny deformation of the DOS, getting broader while the energy gap becomes narrower, until it finally vanishes. The fact that the gap disappears does not mean that the system has lost its magnetic order completely. In fact, no gap is observed for $k_B T/\gamma = 0.3$, even though we still observe partial AFM ordering and a correlation (see Figure 3.13) larger than -0.4 . With regards to the spin density function, we may observe a transitional region between the AFM and the paramagnetic configurations. The aforementioned region is made up magnetic domains that preserve an AFM ordering only locally, and thus contribute to a smaller global correlation.

However, and as already mentioned, a finer MC would require a larger amount of sweeps in order to deal with statistical fluctuations that might arise in the one presented in this report. For instance, at large temperatures the correlation appears to be at around -0.1 , even though we should expect it to lie close to zero. The Strong Law of Large Numbers assure that the sample mean converges to zero, though it does not assert when. Therefore, the exact number of steps necessary to avoid this and other statistical inconsistencies is unknown, mainly because the MC itself is random. Another input value which is reasonable to change is the array of temperatures. For the MC depicted in 3.13, it would have been much more reasonable to consider a finer grid within the interval $0.1 \leq \frac{k_B T}{\gamma} \leq 0.4$ in order to account for sudden changes in the correlation during the phase transition. This would have allowed us to examine the gradual lost of AFM ordering and the magnetic domains of the “pre-metallic” states. This is much more preferable than performing simulations above $\frac{k_B T}{\gamma} = 0.4$, precisely when the system has already become metallic.

For the purpose of future simulations, it may be useful to determine a temperature for which the AFM ordering begins to vanish, and so avoiding making some trials to find out the best region to perform the MC. Recall that, starting from a microstate i with energy E_i at temperature T , the probability to jump to another microstate j with energy E_j is given by the quotient between Boltzmann factors:

$$p_{ij} = e^{\frac{E_j - E_i}{k_B T}} = e^{\frac{\Delta E}{k_B T}} \quad (3.3)$$

Let us consider that i is the AFM state and j is the same one except for a spin that has been flipped. Obviously, j is the closest microstate to i and their energy difference ΔE is the one that has to be overcome by our MC so that the phase transition may begin. Let us estimate the probability α of reaching the microstate j at least once within n thermalization steps X_1, \dots, X_n :

$$\alpha = \mathbb{P}(\exists k: X_k \leq p_{ij}) = 1 - \mathbb{P}(X_1, \dots, X_n > p_{ij}) = 1 - \mathbb{P}(X_1 > p_{ij})^n = 1 - (1 - p_{ij})^n. \quad (3.4)$$

Recall that each random variable is uniformly distributed in $(0, 1)$ ($X_i \sim \mathcal{U}(0, 1)$) as we are using the Metropolis-Hastings algorithm to decide whether the change is accepted or not. Therefore, they are stochastically independent.

Isolating the temperature and expressing both energy and thermal excitation in terms of γ we obtain:

$$\frac{k_B T}{\gamma} = -\frac{\Delta E}{\gamma} \frac{1}{\log(1 - (1 - \alpha)^{1/n})}. \quad (3.5)$$

Whereas the value of ΔE must be determined by just running two simulations, the parameter α is arbitrary. Reasonable choices are $\alpha = 0.95$ or $\alpha = 0.99$. Recall that the value of ΔE is not the same for any pair of parameters U and γ , so it must be calculated any time we change the model we are using. In our case, for $U/\gamma = 2.72$, this difference is around $\Delta E \sim \gamma$. Moreover, recall that the 6 thermalization sweeps correspond, due to the lattice size, to $6 \cdot 100 = 600$ thermalization steps.

$k_B T/\gamma$	α
0.05	$< 10^{-5}$
0.10	0.02687
0.15	0.53423
0.20	0.98269
0.25	0.99998

Table 3.1: α in terms of the thermal excitation.

A quantitative example of the former expressions for $U/\gamma = 2.72$ is given in Table 3.1. We may see that from $k_B T/\gamma \sim 0.20$ onwards it is almost certain that the AFM is not the only accessible microstate. However, as done in Figure 3.13, it is recommendable to start at some value close to $k_B T/\gamma \sim 0.1$ so that there is at least one AFM point on our plot. This procedure may help us to estimate a region where the phase transition should take place, while assessing a temperatures range to make our MC as fine and optimal as possible.

Chapter 4

Conclusions and future work

Let us take a brief but general look at this work and its outcomes, setting up ideas for future contributions to the topic we have dealt with.

The underlying reasons behind the phenomenon of superconductivity are not totally clear for non conventional superconductors, and the BCS theory does not suffice to explain their behaviour. Exploring such a broad and still unknown topic is out of the scope of this work. Instead, we have just focused on describing the electronic structure of the undoped La_2CuO_4 - one of the most relevant high- T_c superconductors - and the importance of the magnetic ordering using a minimalistic model.

Our work has begun by considering a framework suitable for our aim. On the one hand, we realised that our problem may be simplified to a two-dimensional magnetic system, representing the CuO_2 layers of the La_2CuO_4 . We discussed the main orbitals that form the most important bands of our system. Moreover, since these orbitals hybridize, we have been able to computationally describe a CuO_2 layer as a $n \times n$ lattice with periodic boundary conditions and one Wannier orbital per lattice site.

On the other hand, the development of a DFT-based second-principles model has been crucial. Within this model, the DFT Hamiltonian resembles a Hubbard-like model, and hence it is possible to take magnetism into account by means of two parameters: γ and U .

Once the model had been exposed, we started by reproducing the bands using a simple tight-binding model which does not take spin into account. We noted the relevance of the first-order parameter, γ , to account for bonding. After “turning on” the spin, it was necessary to introduce a second parameter U to describe electron-electron interaction.

Before even dealing with magnetic ordering, we aimed to examine how these two parameters determine essential properties our system. Since we may express the DFT Hamiltonian in terms of U/γ , we came to realize that electronic and magnetic interactions are linked with each other by means of the factor U/γ , and that this factor determines whether metallic states can be found or not. As a matter of fact, we estimated a region for U/γ where the desired insulator-metal transition phase can occur.

Subsequently, we introduced the correlation as a way to quantify magnetic ordering. This has allowed us to describe a complex magnetic state with a single number instead of a $n \times n$ matrix. Moreover, this helped us to confirm that AFM configuration is our system’s ground state, whereas the FM one is an energy maximum.

The former steps were necessary to set up the observation of the desired phase transition, requiring a temperature calculation which is not directly possible with DFT. A Monte Carlo method, based on the Metropolis-Hastings algorithm, served this purpose. A computationally limited, though representative simulation has provided enough evidence to assert that the DFT second-principles approach, implemented on SCALE-UP, is able to reproduce such phenomenon.

All these elements, combined and properly used, have served us to reproduce a phase transition which is simultaneous: AFM-paramagnetic and insulator-metal. Needless to say, this have been accomplished by means of a simple model and regardless of phonons and lattice contributions. The fact that this is a simultaneous transition evidences that metallic and magnetic properties are strongly correlated.

As we have already mentioned, this work is restricted to the undoped case, and thus we have not explored appealing states that appear if holes concentration increases, not to mention the superconductor state. In order to fully understand high- T_c superconductivity in La_2CuO_4 , we must be able to explain the whole temperature-doping phase diagram. Achieving this goal would be a natural extension of the approach presented here. Future work should consider adding holes in our system in order to seek characteristic phenomena of intermediate phases, such as exotic holes dispositions (stripes) and the pseudogap region.

Bibliography

- [1] R. K. Wangness. *Electromagnetic Fields*. John Wiley and Sons, 2nd edition, 1986.
- [2] V. Z. Kresin, S. A. Wolf *Fundamentals of Superconductivity* Springer Science+Business Media New York, 1990.
- [3] H. K. Onnes, Leiden Comm. 1911, 119b, 122–124.
- [4] J. Bardeen, L. N. Cooper, and J. R. Schrieffer, *Theory of Superconductivity*, Phys. Rev. 108, 1175 – Published 1 December 1957.
- [5] D. Semenov, I. Kruglov, I. Savkin, A. Kvashnin, A. Oganov *On Distribution of Superconductivity in Metal Hydrides*, arXiv:1806.00865.
- [6] R. Hott, R. Kleiner, T. Wolf, G. Zwicknagl, *Review on Superconducting Materials* , arXiv:1306.0429.
- [7] D. Lee, *Routes to High-Temperature Superconductivity: A Lesson from FeSe/SrTiO₃*, Annual Review of Condensed Matter Physics, Vol. 9:261-282.
- [8] B. Keimer, A. Aharony, A. Auerbach, R. J. Birgeneau, A. Cassanho, Y. Endoh, R. W. Erwin, M. A. Kastner, and G. Shirane *Néel transition and sublattice magnetization of pure and doped La₂CuO₄*. Phys. Rev. B 45, 7430 – Published 1 April 1992.
- [9] M. A. Kastner, R. J. Birgeneau, G. Shirane and Y. Endoh. *Magnetic, transport, and optical properties of monolayer copper oxides* Rev. Mod. Phys., Vol. 70, No. 3, July 1998.
- [10] M. Reehuis, C. Ulrich, K. Prokeš, A. Gozar, G. Blumberg, Seiki Komiya, Yoichi Ando, P. Pattison, and B. Keimer *Crystal structure and high-field magnetism of La₂CuO₄*, Phys. Rev. B 73, 144513 – Published 21 April 2006.
- [11] P. García-Fernández, M. Moreno, and J.A. Aramburu-Zabala, *Electrostatic Control of Orbital Ordering in Noncubic Crystals*, J. Phys. Chem. C 2014, 118, 7554-7561.
- [12] K. Mitsen , O. Ivanenko, *Charge ordering, superconductivity, and stripes in doped La₂CuO₄*, Journal of Experimental and Theoretical Physics 100(6):1082-1093, June 2005.
- [13] D. Haskel, V. Polinger, E.A. Stern *Where do the doped holes go in La_{2-x}Sr_xCuO₄? A close look by XAFS*, AIP Conference Proceedings, 483(1), 241-246, September 1999.
- [14] F. Jensen, *Introduction to Computational Chemistry*, Ed Wiley, Odense, 2007.

- [15] J. D. Patterson, B. C. Bailey, *Solid-State Physics Introduction to the Theory*, Ed. Springer-Verlag, 2007.
- [16] J.A. Aramburu-Zabala. , *Apuntes de Física Cuántica III*, Universidad de Cantabria, curso 2018-2019.
- [17] P. García-Fernández , *Inestabilidades en materiales impurificados*, Tesis Doctoral de la Universidad de Cantabria, septiembre de 2004.
- [18] P. Hohenberg and W. Kohn, *Inhomogeneous Electron Gas*, Phys. Rev. 136, B864 – Published 9 November 1964.
- [19] K. Kohn and L.J. Sham *Self-Consistent Equations Including Exchange and Correlation Effects*, Phys. Rev. 140, A1133 – Published 15 November 1965.
- [20] P. García-Fernández, J. C. Wojdel, J. Íñiguez, and Javier Junquera Phys. Rev. B 93, 195137 – Published 19 May 2016.
- [21] K. Ohno, K. Esfarjani and Y. Kawazoe, *Computational Materials Science, From Ab Initio to Monte Carlo Methods*. Ed. Springer-Verlag Berlin Heidelberg 1999.
- [22] Robert C.P., Casella G. (1999) *The Metropolis—Hastings Algorithm*. In: *Monte Carlo Statistical Methods*. Springer Texts in Statistics. Springer, New York, NY.
- [23] N. Metropolis, A. Rosenbluth, M. Rosenbluth, A. Teller, E. and Teller, *Equations of state calculations by fast computing machines*. J. Chem. Phys., 21(6): 1087–1092, 1953.
- [24] W. Hastings, *Monte Carlo sampling methods using Markov chains and their application*. Biometrika, 57: 97–109, 1970.
- [25] E. Pavarini, E. Koch, R. Scalettar and R. Martin. *The Physics of Correlated Insulators, Metals, and Superconductors*, Lecture notes of the Autumn-School on Correlated Electrons 2017, available in <http://hdl.handle.net/2128/15283>.
- [26] J. Junquera, *Basic concepts of the electronic models*.
- [27] S. Shapiro, M. Wilk, *An analysis of variance test for normality (complete samples)*, Biometrika, Volume 52, Issue 3-4, December 1965, Pages 591–611.

Appendix A

Code implementation

The results of this work have been obtained by means of a combination of Python and SCALE-UP scripts needed to generate both the second-principles model and the lattice, together with the analysis in form of output scripts and plots. This work’s own scripts approximately contain 1700 lines of code. Reasons for choosing Python 3.7 are its intuitiveness and easiness, as this programming language is flexible enough to adapt itself to the purposes and methodology of this work. Moreover, Python presents a large list of libraries that allow us to perform mathematical operations and handle data in form of matrices (*numpy* and *math*), as well as proper graphical representation (*matplotlib.pyplot*) and interpolation (*scipy*). The libraries *os* and *sys* have been used too. A brief summary of the scripts needed to run SCALE-UP is given in the following table:

2d_hubbard.orbocc	Script for the two-dimensional lattice. Each lattice point is assigned two spin channels set at (0.5,0.5) by default. Spin up and down is achieved by inserting (0.5,-0.5) and (-0.5,0.5), respectively.
2d_hubbard.xml	SCALE-UP second-principles model. It contains information about the system’s geometry and the hamiltonian’s parameters (γ and U).
2d_hubbard.fdf	SCALE-UP input file. It reads both the model from the .xml script and the lattice configuration from the .orbocc file. Other parameters shall be specified as well, such as k-sampling, grid of reciprocal space, SCF threshold, numerical tolerance, etc.

Table A.1: Summary of the three scripts needed to run a SCALE-UP second-principles simulation.

Table A.1 summarizes the three scripts used by SCALE-UP to run a second-principles simulation. A tight-binding model may be also achieved by setting the second-principles parameters U and I to zero in the .xml script. As already mentioned in Chapter 2, resembling the Hubbard model requires $I = U$.

After running a SCALE-UP simulations, several files appear in the working directory. In our case, and for the sake of clarity, all of them excepting the .txt output (name specified in the .fdf) are preceded by a string *_2d_hubbard_FINAL*. Some of these files are:

- *_2d_hubbard_FINAL.orbocc*: Lattice magnetic ordering after simulation.
- *_2d_hubbard_FINAL.bands*: Output file prepared as input to plot the bands.
- *_2d_hubbard_FINAL.ener*: Output file prepared as input to plot the DOS.

- output: .txt file which contains all the information regarding the SCF convergence process. As a matter of fact, we have been mainly interested in the system's total energy.

DOS and bands can be automatically plotted by means of the script `scaup_utils.py`, already provided with the SCALE-UP code. However, since electronic properties along the Monte Carlo simulation are computed as the average of several MC steps, we have created our own functions to plot bands and DOS in terms of this output. Python scripts are summarized in Table A.2.

Orden.py	This Python script generates a 2d lattice and saves it with a <i>name.orbocc</i> syntax. The spin configuration can be passed via command line (library <code>sys</code>) or generated randomly. The latter has been always the case except for the intentionally considered AFM and FM configurations.
Plot3d.py	Given a set of values of U and γ , this script calculates the difference between the AFM and the FM configurations and plots it on a $U - \gamma$ grid to produce the 3d plot of the Figure 3.7. The corresponding 2d plot of the same figure and the computing times (Figure 3.8) are also produced.
Calculos.py	This script creates .xml and .fdf files for different values of U/γ . A previously indicated number of simulations is performed. After each one, the script saves all the aforementioned output files, as well as the initial configuration (.orbocc) in a reference folder.
Correlacion.py	This file reads both spin correlation and energy from the files generated by <code>Calculos.py</code> to produce the fits and histograms in Figures 3.10 and 3.11. It also adds the AFM and FM configurations.
MC.py	<p>This script, provided with a large number of functions, performs the Monte Carlo simulation. <code>MC.py</code> creates a random lattice at each step by means of <code>Orden.py</code> and goes through the algorithm described in Chapter 2. The rest of the Python functions contained in this script are used to:</p> <ul style="list-style-type: none"> • Perform lattice perturbations (spin flipping) for the MC. • Calculate correlation of current state. • Plot DOS. • Plot spin correlation as a function of $k_B T/\gamma$ (Figure 3.13). • Plot a spin map in greyscale (Figure 3.14). <p>While the MC simulation is running, this script writes in a .txt file all the data regarding every single step. In particular, this file contains information about whether the state is updated, the current temperature, energy and correlation (normalized) as well as general information about the whole simulation itself.</p>

Table A.2: Summary of the main Python scripts used to produce the results of our works. Note that minor scripts used for the purpose of testing our model and making fast trials are not included in this table. Some scripts that were thought to begin working with doped systems have been also created, though not implemented as the beginning of the COVID-19 pandemic lockdown hindered continuing with this work.

